Response to Request for Additional Information for the Review of

COBRA-FLX: A Core Thermal-Hydraulic Analysis Code

Topical Report

January 2011

AREVA NP Inc.

Responses to Requests for Additional Information (RAI)

Request 1

(Verification of Solution Methods) The documentation provided in the above mentioned report does not fully demonstrate that the two solution methods under review (referred to as the SCHEME-Pressure (P) solution method and the Pressure-Velocity (PV) solution method, or more simply as the (P) solution method and the (PV) solution method), yield the same results for the same boundary conditions and model geometry. Section 5.1 *Conservation of Mass and Energy*, does not provide a meaningful comparison of the results obtained with the two solution methods for the four different modeling geometries considered in this analysis. For this evaluation to be complete, it is necessary to show that the two solution methods yield the same results, within convergence limits, for the same geometric models by comparison of flow and enthalpy distributions in both the radial and axial directions. Particular attention should be given to comparisons of the results obtained for the hot subchannel in the hot assembly.

Response 1:

The consistency of the local conditions between the SCHEME-Pressure (P) and the Pressure-Velocity (PV) solution methods is demonstrated by comparing steady-state results from the 12-, 52-, 75- and 7083-channel models. The comparisons are based on all the axial control volumes in the limiting DNB channel (channel with the minimum DNBR), a channel adjacent to the limiting DNB channel, and a channel two fuel pin pitches away from the limiting DNB channel. Figure Q1-1 shows the relationship of the three channels used in this comparison.

Figure Q1-1: Subchannel Identification Around The Limiting Channel

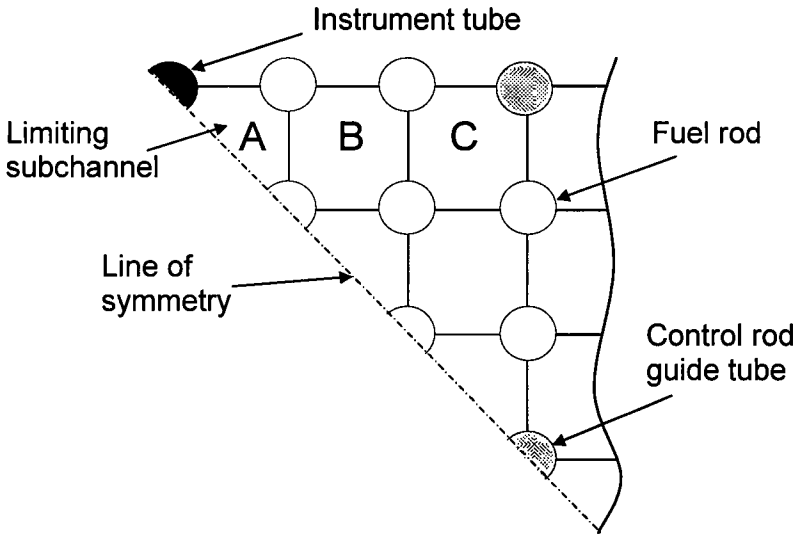

Figure 5-18, on page 5-24, shows the PV prediction of axial mass flux responding earlier to hydraulic resistances relative to the P solution. As stated on page 5-24 this difference is attributed to the PV solution method's use of a staggered axial mesh to account for the position of the momentum control volumes as discussed throughout Section 2.3.2 and defined in Figure 2-16. Figure Q1-2 contains a comparison of the P and PV solutions axial control volumes for the axial momentum equation.

If the spacer hydraulic resistance is placed in the lower half of the P solution method axial control volume (between x_J and $x_J + \Delta x_+$ in Figure Q1-2), then the P solution method will place the axial pressure loss in the control volume between x_J and x_{J+1}. For the same user-input placement of the hydraulic resistance, the PV solution method will place the pressure loss in the upstream P solution method control volume (x_{J-1} and x_J in Figure Q1-2) due to the staggered axial momentum PV solution method control volume (between $x_J - \Delta x_-$ and $x_J + \Delta x_+$ in Figure Q1-2). In order to align the axial pressure drops between the P and PV solution methods' axial control volumes, the spacer grid hydraulic resistance is placed in the upper half of the P solution method axial control volume (between $x_J + \Delta x_+$ and x_{J+1} in Figure Q1-2).

Figure Q1-2: Subchannel Control Volume

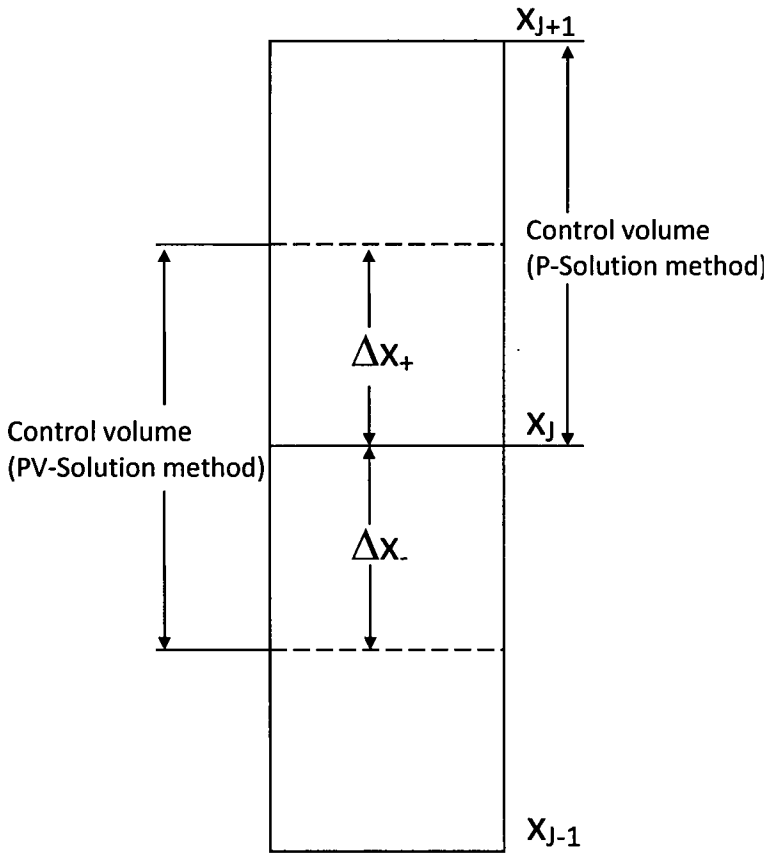

Table Q1-1 contains a comparison of the axial and radial differences between the P and PV solution methods for the four different channel models, based on the spacer hydraulic resistance in the lower half of the P solution method axial control volume. This placement is consistent with the analysis results shown in Figure 5-18.

Table Q1-1: Axial Flow Rate and Enthalpy Comparison Between P and PV Solution Methods for the Three Subchannels

Number of Channels in Model	Time (sec)	Subchannel ID (Fig. Q1-1)	Average Axial Absolute Difference, % $\left\lvert\left(\frac{P - PV}{P}\right)\times 100\right\rvert$		Maximum Axial Absolute Difference, % $\left\lvert\left(\frac{P - PV}{P}\right)\times 100\right\rvert$	
			Axial Enthalpy	Axial Flow Rate	Axial Enthalpy	Axial Flow Rate
12	0	A	0.0026%	0.2218%	0.0101%	2.7778%
52	0	A	0.0085%	0.2158%	0.0124%	2.7638%
75	0	A	0.0084%	0.2336%	0.0124%	2.8381%
7083	0	A	0.0108%	0.2707%	0.0159%	2.8286%
12	0	B	0.0022%	0.1602%	0.0068%	2.2476%
52	0	B	0.0079%	0.1666%	0.0185%	1.7235%
75	0	B	0.0082%	0.1632%	0.0191%	1.7248%
7083	0	B	0.0100%	0.2103%	0.0206%	2.1691%
12	0	C	0.0037%	0.1997%	0.0136%	2.2680%
52	0	C	0.0037%	0.1997%	0.0150%	2.2955%
75	0	C	0.0096%	0.2205%	0.0156%	2.2965%
7083	0	C	0.0102%	0.2318%	0.0176%	2.3701%

Results from Table Q1-1 show that, in the case of P versus PV solution methods comparisons, the mean average percentage difference for the axial flow rate and enthalpy remain less than 0.3 %, and maximum absolute percentage difference is ~3% for axial flow and ~0.2% for enthalpy, respectively.

Table Q1-2 provides a comparison of results for the P solution with the spacer hydraulic resistance in the lower half of the control volume and results for the P solution with the resistance in the upper half of the control volume. Table Q1-2 demonstrates that there is no difference, to within the number of digits of output, in the P solution-based predictions on the location of the spacer resistance.

Table Q1-2: Axial Flow Rate and Enthalpy Comparison Between P and P (with spacer hydraulic resistances placed in the upper half of the control volumes) Solution Methods

Number of Channels in Model	Time (sec)	Subchannel ID (Fig. Q1-1)	Average Axial Absolute Difference, % $\left\lvert\left(\frac{P - \text{P(shifted spacer)}}{P}\right)\times 100\right\rvert$		Maximum Axial Absolute Difference, % $\left\lvert\left(\frac{P - \text{P(shifted spacer)}}{P}\right)\times 100\right\rvert$	
			Axial Enthalpy	Axial Flow Rate	Axial Enthalpy	Axial Flow Rate
12	0	A	0.0000%	0.0000%	0.0000%	0.0000%
12	0	B	0.0000%	0.0000%	0.0000%	0.0000%
12	0	C	0.0000%	0.0000%	0.0000%	0.0000%

Table Q1-3 provides a comparison of the P solution, with the spacer hydraulic resistance in the lower half of the control volume, and PV solution with the resistance in the upper half of the control volume.

Table Q1-3: Axial Flow Rate and Enthalpy Comparison Between P and PV (with spacer hydraulic resistances placed in the upper half of the control volumes) Solution Methods

Number of Channels in Model	Time (sec)	Subchannel ID (Fig. Q1-1)	Average Axial Absolute Difference, % $\left\lvert\left(\frac{P - \text{PV}}{P}\right)\times 100\right\rvert$		Maximum Axial Absolute Difference, % $\left\lvert\left(\frac{P - \text{PV}}{P}\right)\times 100\right\rvert$	
			Axial Enthalpy	Axial Flow Rate	Axial Enthalpy	Axial Flow Rate
12	0	A	0.0036%	0.0404%	0.0129%	0.2646%
52	0	A	0.0009%	0.0514%	0.0055%	0.3518%
75	0	A	0.0006%	0.0491%	0.0039%	0.3512%
7083	0	A	0.0025%	0.0698%	0.0046%	0.3521%
12	0	B	0.0039%	0.0430%	0.0077%	0.2157%
52	0	B	0.0035%	0.0465%	0.0068%	0.2222%
75	0	B	0.0035%	0.0471%	0.0075%	0.2597%
7083	0	B	0.0036%	0.0744%	0.0106%	0.2231%
12	0	C	0.0027%	0.0413%	0.0179%	0.2196%
52	0	C	0.0027%	0.0413%	0.0098%	0.2197%
75	0	C	0.0028%	0.0443%	0.0080%	0.2197%
7083	0	C	0.0042%	0.0748%	0.0141%	0.3062%

A comparison of the results from Tables Q1-2 and Q1-3 indicates that placing the spacer hydraulic resistance in the top half of the P solution control volume decreases the axial and radial enthalpy and flow differences between the P and PV solution methods. Figures Q1-3 through Q1-6 show the axial flow rate profiles for the three subchannels identified in Figure Q1-1 for the 12-channel model. These three figures visually verify that the P and PV solution methods are generating the same solution to within 0.4 percent. Figure Q1-3 also shows that the differences between P and the Figure 5-18 PV solution occur at the spacer grid axial control volumes. Figures Q1-4 through Q1-6 compares the axial enthalpy profiles for the three subchannels and visually indicates that the P and PV solution methods agree to within 0.05 percent.

Figure Q1-3: Axial Flow Rate Comparisons for Subchannel A (12 Channel Model)

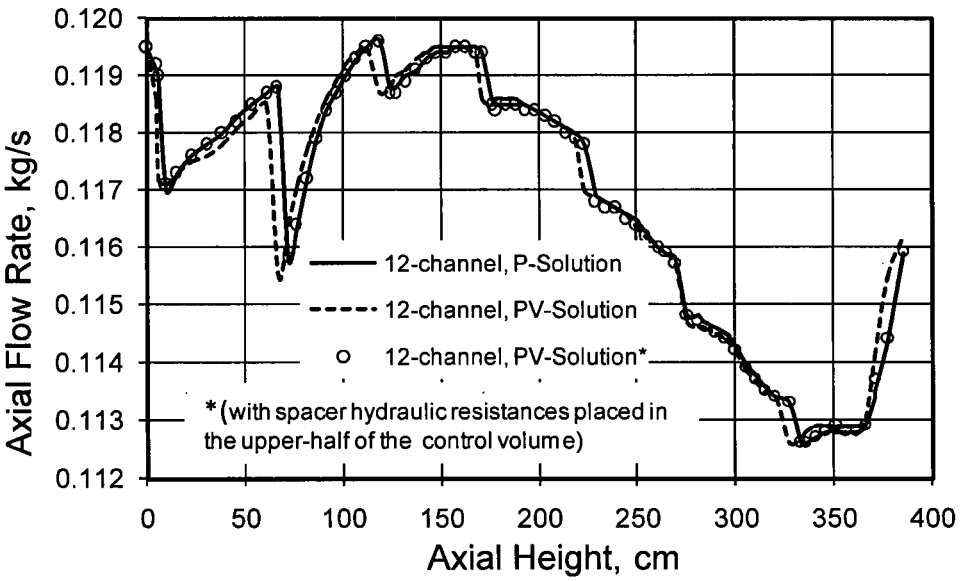

Figure Q1-4: Axial Flow Rate Comparisons for Subchannel B (12 Channel Model)

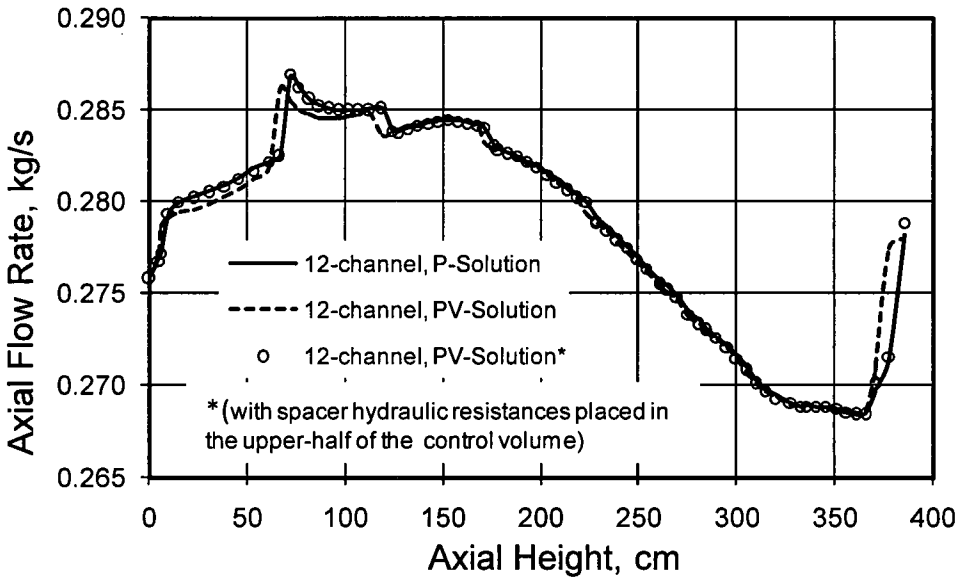

Figure Q1-5: Axial Flow Rate Comparisons for Subchannel C (12 Channel Model)

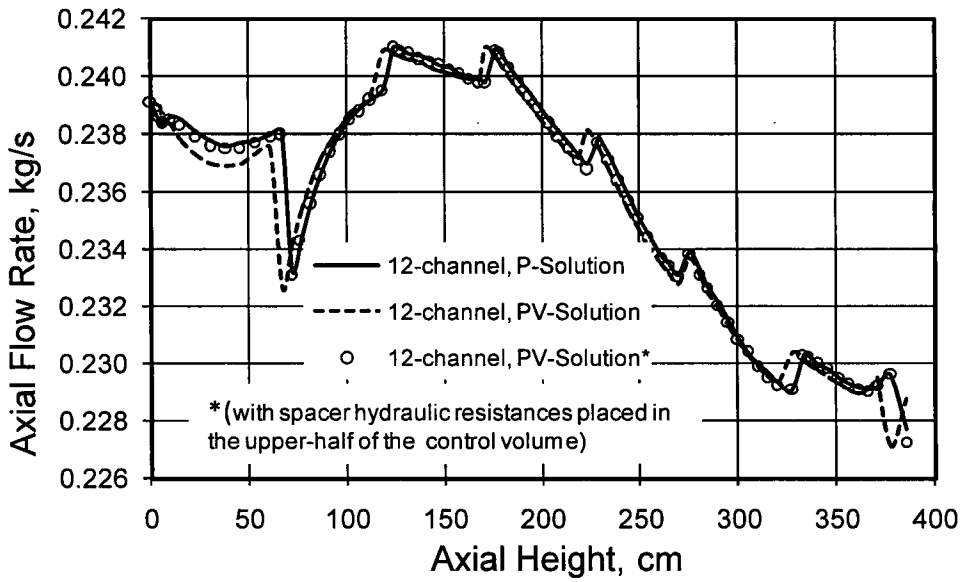

Figure Q1-6: Axial Enthalpy Comparisons for Subchannel A (12 Channel Model)

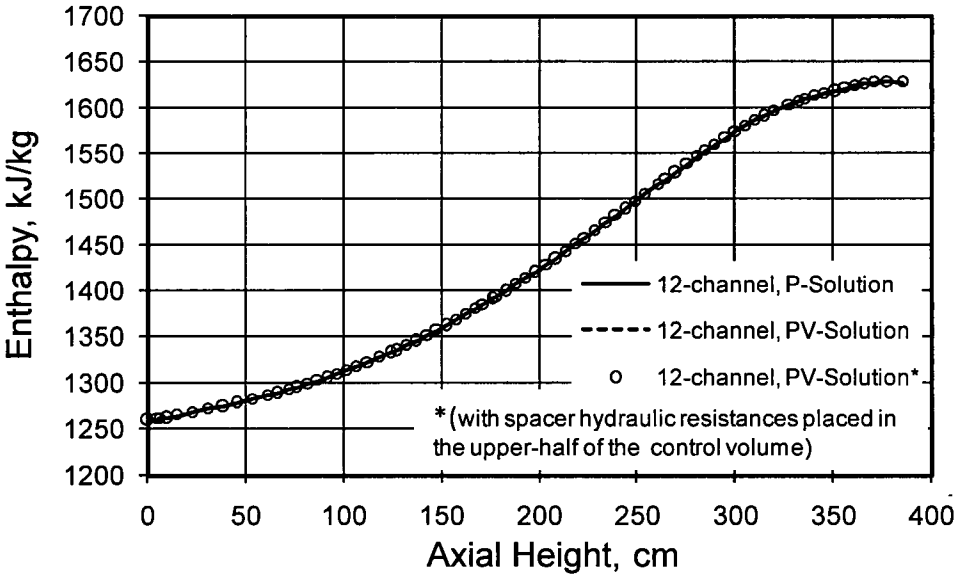

Figure Q1-7: Axial Enthalpy Comparisons for Subchannel B (12 Channel Model)

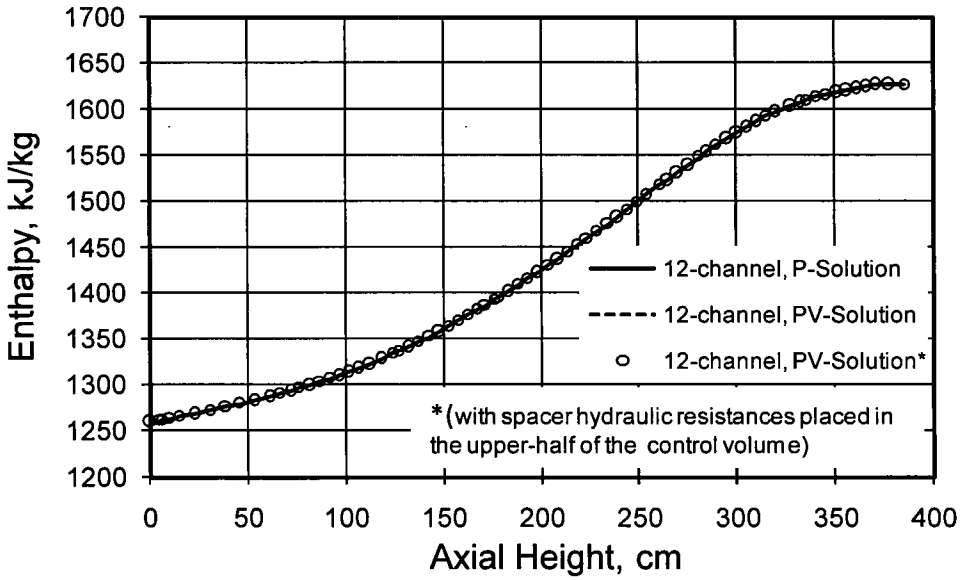

Figure Q1-8: Axial Enthalpy Comparisons for Subchannel C (12 Channel Model)

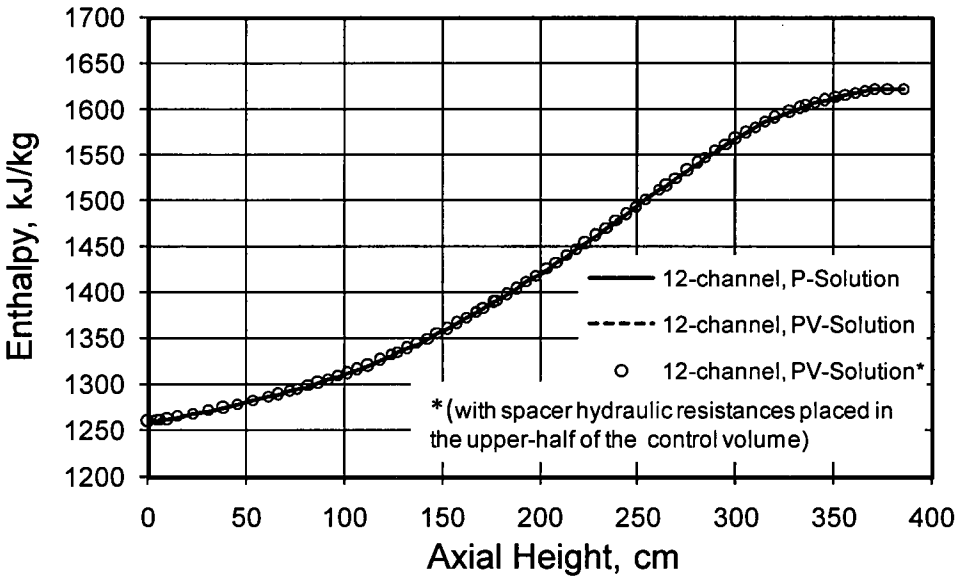

The maximum difference in enthalpy and flow between P and PV results was less than 0.08 percent and 0.4 percent, respectively for the three subchannels in Figure Q1-1 over a range of model sizes. These comparisons were based on placing the spacer hydraulic resistance in the top half of the P solution control volume, which allows the axial pressure profile in P and PV to agree. These comparisons verify that the SCHEME-Pressure (P) and Pressure-Velocity (PV) solution methods yield results to within 0.4 percent for the same boundary conditions and model geometry.

Based on the results of the comparisons, AREVA is adopting the user requirement that hydraulic resistances for spacer grids be positioned at an axial position corresponding to the upper-half of the control volume. This will lead to more consistent results between P and PV solution methods based analyses.

Request 2

(Verification of Solution Methods) Section 5.4, p. 5-26 and 5-27: It is not explicitly stated in Table 1-1 (p. 1-7) that the optional SOR solver (described in Section 2.3.1.4.1) and the [ ] SOR solver (described in Section 2.3.1.4.2) are to be included in the scope of this review. However, on p. 5-27, the report states that "The differences between the results of these SOR methods with the P-solution as opposed to the P solution are insignificantly small.... Therefore, the P solution results and conclusions supported by the Section 5.4 validation would be applicable to the SOR methods." Provide qualitative and quantitative technical justification to justify including the SOR solvers as part of the review of the (P) solution method. For this evaluation to be complete, it is necessary to show that

a. the (P) solution method with its original solver and the two SOR solvers yield the same results, within convergence limits, for the range of geometric models evaluated in Section 5.1 by comparison of predicted flow and enthalpy distributions in both the radial and axial directions.

Response 2:

COBRA-FLX contains three solution algorithms for the P solution method. The three algorithms are: direct solution of the matrix system of equations; use of an SOR algorithm (as defined in Section 2.3.1.4.1); and a [ ] SOR algorithm (as defined in Section 2.3.1.4.2).

The 4 pump coastdown transient used in Section 5.7.2.1 served as the basis for a comparison of the 12-, 75-, and 7083-channel models for the three different P solution algorithms. The same three subchannels used in Figure Q1-1 were used in this comparison. Although the full transient was analyzed for each of the three different channel models, only the initial time step (0 seconds) and the 3.4 second time step results are used in the comparison of the direct, SOR, and [ ] SOR algorithms. The 3.4 second time step corresponded to the transient minimum DNBR.

Tables Q2-1 and Q2-2 contain a comparison of the three models at the three different subchannel locations for the two time steps and over all axial control volumes. In Tables Q2-1 and Q2-2 the comparisons were based on the number of significant figures of output from

COBRA-FLX. Thus, a difference of 0.0% indicates that in terms of the output the results are identical.

Table Q2-1: Axial Flow Rate and Enthalpy Comparison Between P and SOR Solution Methods

Number of Channels in Model	Time (sec)	Subchannel ID (Fig. Q1-1)	Average Axial Absolute Difference, % $\left\|\left(\frac{P - PV}{P}\right)\times 100\right\|$		Maximum Axial Absolute Difference, % $\left\|\left(\frac{P - PV}{P}\right)\times 100\right\|$	
			Axial Enthalpy	Axial Flow Rate	Axial Enthalpy	Axial Flow Rate
12	0	A	0.0000%	0.0000%	0.0000%	0.0000%
75	0	A	0.0000%	0.0000%	0.0000%	0.0000%
7083	0	A	0.0000%	0.0000%	0.0000%	0.0000%
12	3.4	A	0.0000%	0.0000%	0.0000%	0.0000%
75	3.4	A	0.0000%	0.0000%	0.0000%	0.0000%
7083	3.4	A	0.0000%	0.0000%	0.0000%	0.0000%
12	0	B	0.0000%	0.0000%	0.0000%	0.0000%
75	0	B	0.0000%	0.0000%	0.0000%	0.0000%
7083	0	B	0.0000%	0.0000%	0.0000%	0.0000%
12	3.4	B	0.0000%	0.0000%	0.0000%	0.0000%
75	3.4	B	0.0000%	0.0000%	0.0000%	0.0000%
7083	3.4	B	0.0000%	0.0000%	0.0000%	0.0000%
12	0	C	0.0000%	0.0000%	0.0006%	0.0000%
75	0	C	0.0000%	0.0000%	0.0000%	0.0000%
7083	0	C	0.0000%	0.0000%	0.0000%	0.0000%
12	3.4	C	0.0000%	0.0000%	0.0000%	0.0000%
75	3.4	C	0.0000%	0.0000%	0.0000%	0.0000%
7083	3.4	C	0.0000%	0.0000%	0.0000%	0.0000%

Table Q2-2: Axial Flow Rate and Enthalpy Comparison Between P and [ ] SOR Solution Methods

Number of Channels in Model	Time (sec)	Subchannel ID (Fig. Q1-1)	Average Axial Absolute Difference, % $\left\|\left(\frac{P - PV}{P}\right)\times 100\right\|$		Maximum Axial Absolute Difference, % $\left\|\left(\frac{P - PV}{P}\right)\times 100\right\|$	
			Axial Enthalpy	Axial Flow Rate	Axial Enthalpy	Axial Flow Rate
12	0	A	0.0000%	0.0000%	0.0000%	0.0000%
75	0	A	0.0000%	0.0000%	0.0000%	0.0000%
7083	0	A	0.0000%	0.0000%	0.0000%	0.0000%
12	3.4	A	0.0000%	0.0000%	0.0000%	0.0000%
75	3.4	A	0.0000%	0.0000%	0.0000%	0.0000%
7083	3.4	A	0.0000%	0.0000%	0.0000%	0.0000%
12	0	B	0.0000%	0.0000%	0.0000%	0.0000%
75	0	B	0.0000%	0.0000%	0.0000%	0.0000%
7083	0	B	0.0000%	0.0000%	0.0000%	0.0000%
12	3.4	B	0.0000%	0.0000%	0.0000%	0.0000%
75	3.4	B	0.0000%	0.0000%	0.0000%	0.0000%
7083	3.4	B	0.0000%	0.0000%	0.0000%	0.0000%
12	0	C	0.0000%	0.0000%	0.0000%	0.0000%
75	0	C	0.0000%	0.0000%	0.0000%	0.0000%
7083	0	C	0.0000%	0.0000%	0.0000%	0.0000%
12	3.4	C	0.0000%	0.0000%	0.0000%	0.0000%
75	3.4	C	0.0000%	0.0000%	0.0000%	0.0000%
7083	3.4	C	0.0000%	0.0000%	0.0000%	0.0000%

Figures Q2-1 through Q2-3 show the axial flow rates for the three subchannels used as the basis of the comparison in Figure Q1-1.

Figure Q2-1: Axial Flow Rate Comparisons for Subchannel A (12 Channel Model)

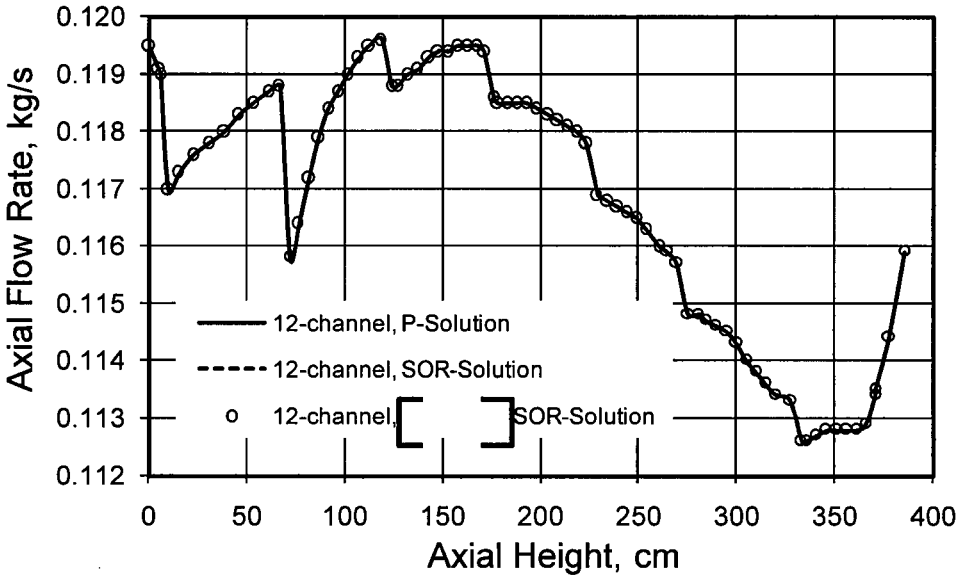

Figure Q2-2: Axial Flow Rate Comparisons for Subchannel B (12 Channel Model)

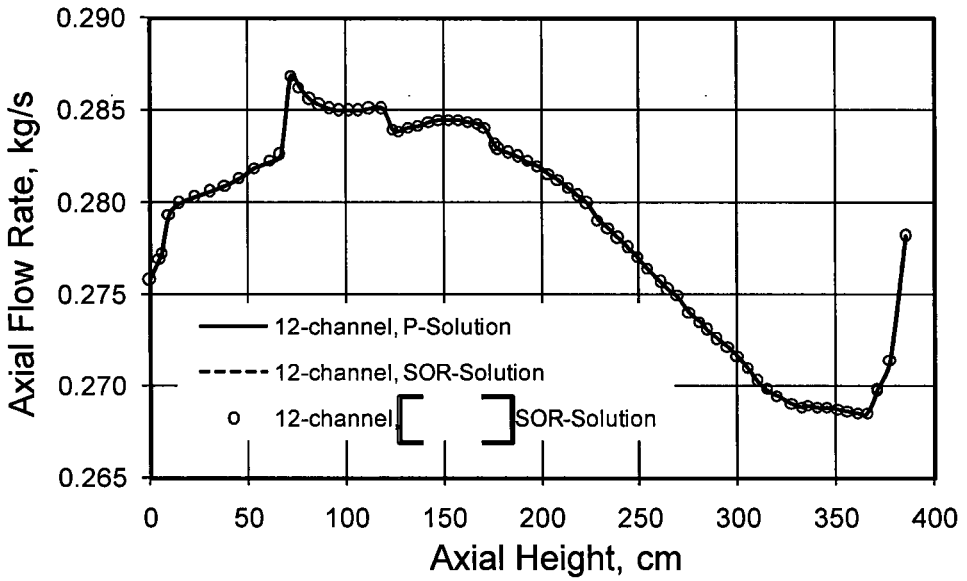

Figure Q2-3: Axial Flow Rate Comparisons for Subchannel C (12 Channel Model)

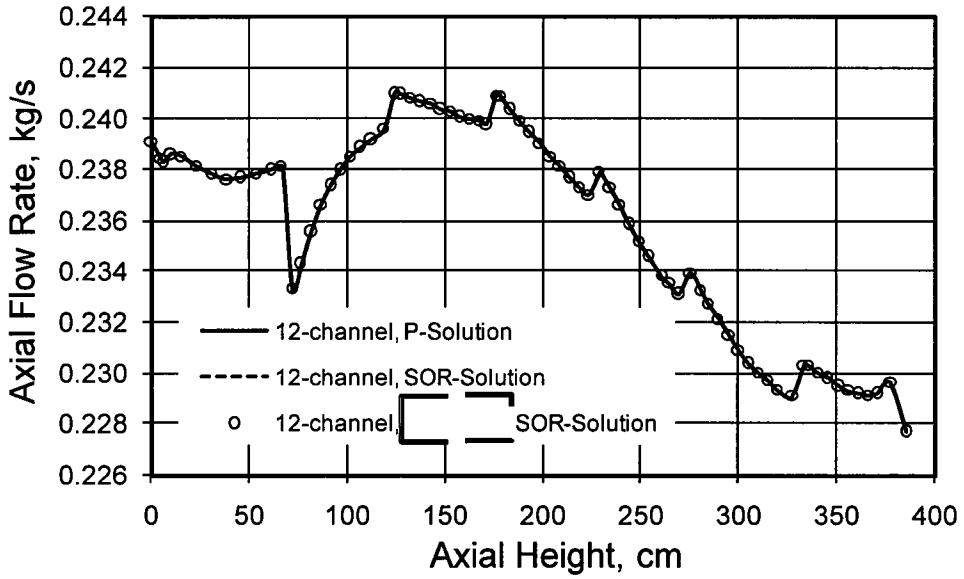

These comparisons of the predicted flow and enthalpy distributions in both the radial and axial directions for three different subchannels verify that the three P solution algorithms produce the same results to within the number of significant digits of output.

Request 3

(Validation of Solution Methods) Section 5.2.1 *Inter-Bundle Diversion Cross-Flow Tests*, does not provide a meaningful comparison to the measured data for the results obtained with the different solution methods in the COBRA-FLX code. Further, the use of a geometry model in which the test section is represented with a single channel per bundle does not provide results demonstrating "that the fluid flow solution, on the scale of individual fuel assemblies *modeled as channels to the finer scale of individual subchannels modeled as channels* [italics added], is reliable for use for the type of flow redistributions encountered in core analysis", as stated in Section 5.2, p. 5-4. For this evaluation to be complete, it is necessary to show that

a. the two solution methods yield the same results for the test cases where both methods are applicable

b. each solution method yields results that are in good agreement with the measured data; in this case, pressure at measured axial locations, as reported on p. 5-4.

c. good agreement with the measured data can be obtained with detailed subchannel models of the test section, as well as with models in which a test bundle is represented with only a few channels or a single channel.

Response 3:

The discussion of the Inter-Bundle Diversion Cross-Flow (IBDCF) tests in Section 5.2.1, modeled with COBRA-FLX using two or four channels, was intended to demonstrate the adequacy of COBRA-FLX for predicting only bundle-scale type thermal-hydraulic characteristics across a broad range of inlet axial flow variations. The absence of the italicized parenthetical text shown below, from a statement extracted from Section 5.2.1, leads to an unintended implication for the use of the IBDCF tests that was appropriately recognized during the Technical Review and reflected in this RAI.

"These two experiments (*collectively*) reflect several Separate Effects Tests (SETs) that are used to demonstrate that the fluid...".

A more detailed comparison of COBRA-FLX's two solution methods for predicting thermal-hydraulic conditions in the asymmetric inlet flow tests is presented in Figure Q3-1 through Figure Q3-6. These figures exhibit the COBRA-FLX predictions of axial velocity ratios and cross flow velocities versus axial location as compared to the experiment-based results for three inlet flow asymmetries, V_2 / V_1 = 0.75 (Test 138), 0.50 (Test 134), and 0.00 (Test 147). As discussed on pg. 5-9 of Section 5.2.1, the COBRA-FLX simulation of the inlet blocked bundle Test 147 used two channels for each bundle, for a total of four channels as opposed to the single channel per bundle used for the twelve less asymmetric tests. The use of smaller channel sizes was necessary for Test 147 to better accommodate the influence of the more severe asymmetric inlet axial velocities and the potential for reverse flow. This demonstration towards finer resolution modeling, although not as detailed as the requested full subchannel-based simulation, does show that COBRA-FLX exhibits acceptable predictive capability for severe asymmetric flow conditions

Upon receipt of this RAI, AREVA did attempt to locate the original fuel assembly experimental pressure data from the 1974 testing period to perform a direct comparison of the pressure measurements to COBRA-FLX predictions. Unfortunately, the original pressure data have not been located to establish a full subchannel-based evaluation. It was AREVA's intent to utilize the MARIGNAN test comparison in Section 5.2.2 to validate the subchannel-based COBRA-FLX predictive capability since local subchannel flow velocities were measured within individual subchannels of the test bundle structures at key locations for observing the influence of large cross flow velocities. The COBRA-FLX validation process using the IBDCF tests was consistent with the IBDCF-based process used for the LYNX1 code (Section 7.2 of Reference Q-A) and LYNXT code (Section 6.1.1 of Reference Q-B)

The two COBRA-FLX solution methods, P and PV, yield similar results from the test cases where both solution methods are applicable as observed in Table 5-2 and in Figures Q3-1 through Q3-4. These same figures also show the two solution methods provide predictive results that agree well with the experiment-based results. The PV-solution method also agrees well with the experiment-based results for the severe inlet velocity asymmetry case as shown in Figures Q3-5 and Q3-6.

Figure Q3-1: Axial Velocity Ratios versus Axial Elevation using COBRA-FLX and Experiment-based Results for IBDCF Test 138 (Inlet Velocity Ratio of 0.75 between Bundles)

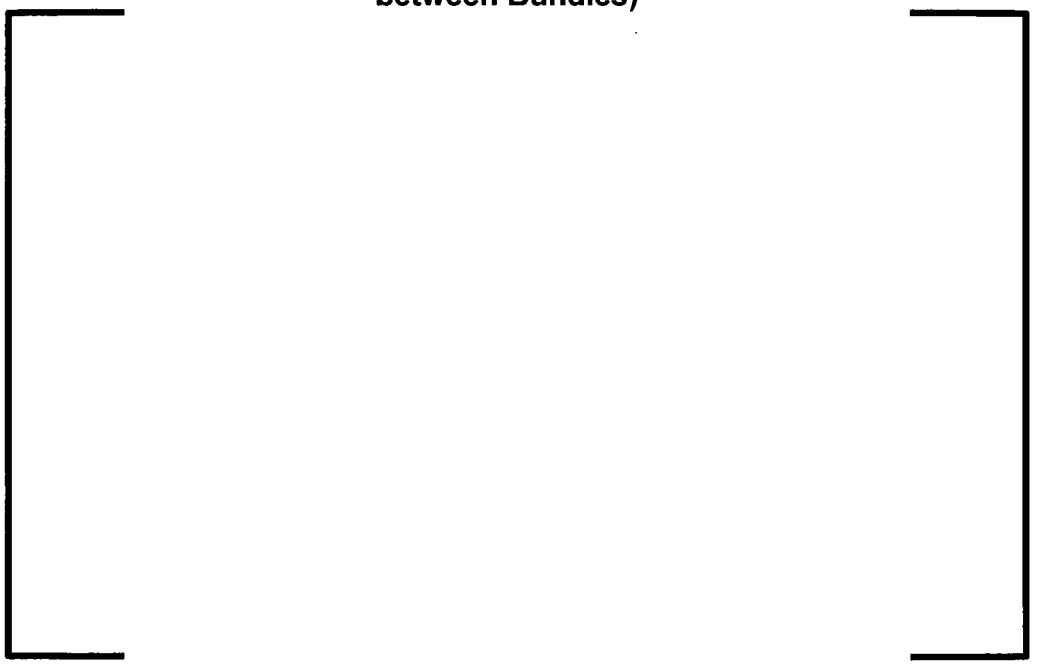

Figure Q3-2: Crossflow Velocity versus Axial Elevation using COBRA-FLX and Experiment-based Results for IBDCF Test 138 (Inlet Velocity Ratio of 0.75 between Bundles)

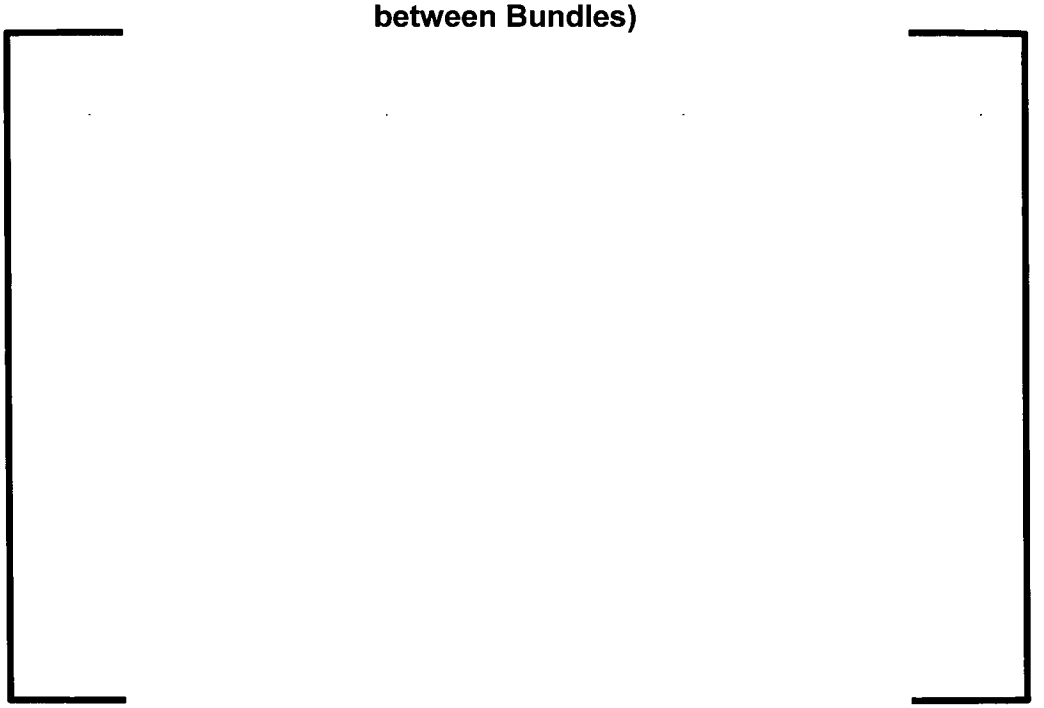

Figure Q3-3: Axial Velocity Ratios versus Axial Elevation using COBRA-FLX and Experiment-based Results for IBDCF Test 134 (Inlet Velocity Ratio of 0.50 between Bundles)

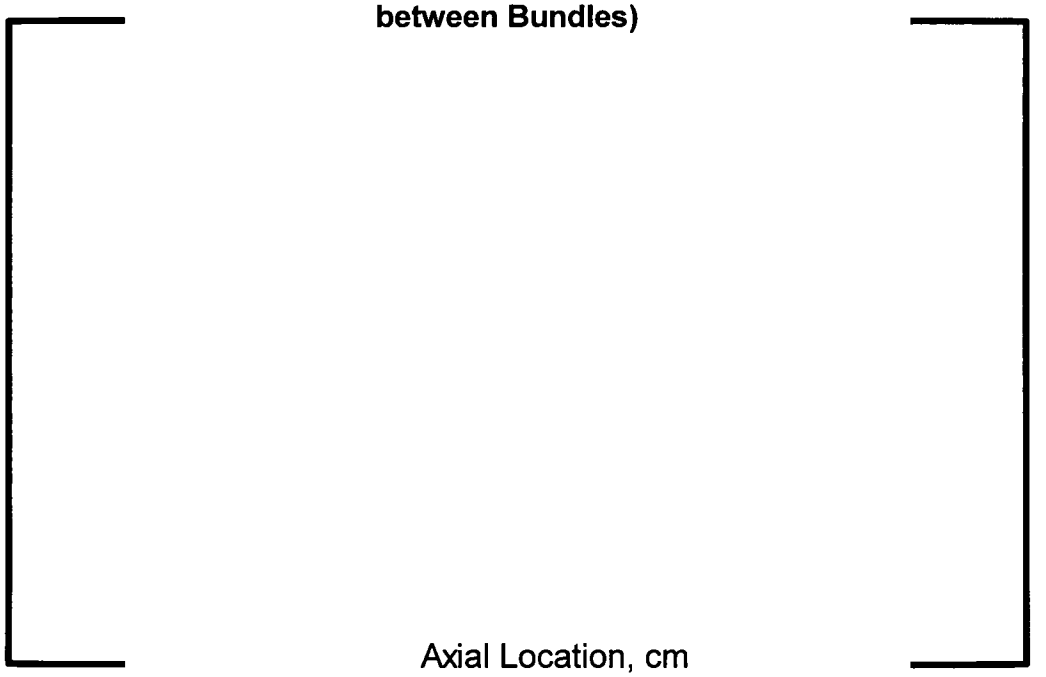

Figure Q3-4: Crossflow Velocity versus Axial Elevation using COBRA-FLX and Experiment-based Results for IBDCF Test 134 (Inlet Velocity Ratio of 0.50 between Bundles)

Figure Q3-5: Axial Velocity Ratios versus Axial Elevation using COBRA-FLX and Experiment-based Results for IBDCF Test 147 (Inlet Velocity Ratio of 0.0 between Bundles)

Figure Q3-6: Crossflow Velocity versus Axial Elevation using COBRA-FLX and Experiment-based Results for IBDCF Test 147 (Inlet Velocity Ratio of 0.0 between Bundles)

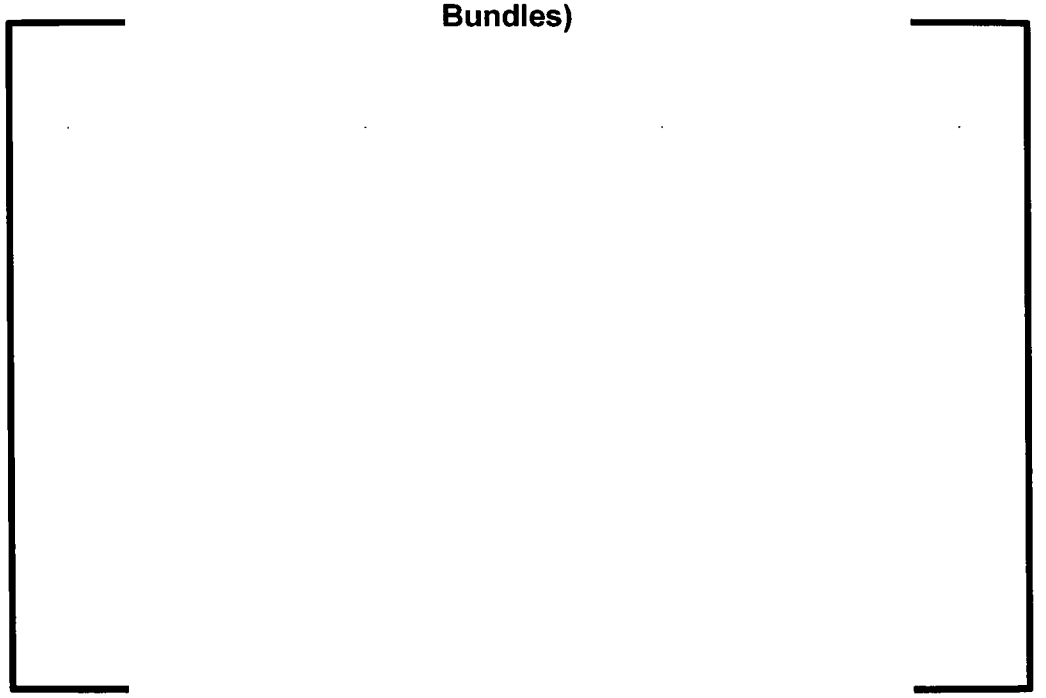

Request 4

(Validation of Solution Methods) Section 5.2.1, p. 5-8: The discussion of the appropriate selection of the crossflow resistance factor for different channel sizes and different inlet flow profile conditions is incomplete and suggests potential problems when developing input models for reactor cores using varying channel sizes from subchannels to large channels encompassing entire fuel bundles or multiple bundles. It is insufficient to simply note that "The COBRA-FLX user is responsible to select the appropriate flow solution method and crossflow resistance factor whenever encountering severe flow differences during application."

a. What criteria were used to select the value of K_{ij} = 4.0 for the severe inlet flow profile conditions of Test 147 of the IBDCF series?

b. Are these criteria generally applicable to all assembly geometries and level of detail in channel modeling?

c. How and where are these criteria documented?

Response 4:

As in Test 147 (severe inlet flow asymmetry) where the axial flow is small and potentially negative, the transverse momentum equation becomes more significant in comparison to the axial momentum equation. Thus, the crossflow resistance (K_{ij}) becomes a more significant factor in the COBRA-FLX calculations. This is demonstrated by comparing the agreement of the COBRA-FLX axial velocity ratios in Table 5-2 (based on the standard high axial flow K_{ij}=0.15) and Table 5-3 (based on a recommended low axial flow K_{ij}=4.0). The use of a low axial flow K_{ij} in the COBRA-FLX topical report is a demonstration of the process that would typically be used and not the definition of specific criteria for all fuel assembly designs and flow conditions.

The criteria used to set the K_{ij} was the best axial mean value of the COBRA-FLX to predicted test velocity ratios for all of the IBDCF tests. The changes in the K_{ij} for the high inlet velocity ratio tests (0.50 and above) were less than 1.0 percent. The sensitivity of the K_{ij} to the mean axial velocity ratio in shown in Table Q4-1.

Table Q4-1: K_{ij} Sensitivity for IBDCF Test 147

For this application a K_{ij} of 4.0 was determined to be the optimal value. A similar process would be followed for other fuel assembly designs if the test data existed. In the absence of test data the IBDCF tests would be used to set the low flow K_{ij} and the axial flow at which a low flow K_{ij} would be used. In the case of the IBDCF tests the axial flow at which K_{ij} becomes an important input when the axial velocity ratio between two adjacent channel is less than 0.5.

The criteria that is used to determine the optimal K_{ij} is that the selected value will produce the best agreement to the test data over the range of flows being evaluated. The criteria are applicable to a specific fuel design, with the applicability being justified on by the end user of COBRA-FLX.

Request 5:

(Validation of Solution Methods) Section 5.2.2 *MARIGNAN Crossflow Tests*, is incomplete and does not provide a meaningful comparison to the measure data for the results obtained with the different solution methods in the COBRA-FLX code. For this evaluation to be complete, additional information is needed to describe the tests, the COBRA-FLX model, and the comparison of the code results to the measured data. Specifically, it is necessary to show

a. the inlet flow conditions and operating temperature(s) for the tests used in the evaluation

b. the geometry model used for the COBRA-FLX analyses

c. the results obtained with the (P) and (PV) solution methods, for a range of test conditions, compared to the measured data

d. direct comparison of results of each solution method with the measured data, instead of the normalized values of V/V_{mean} presented in Figures 5-12 through 5-15

e. comparison of code results with measured data over the full range of 21 axial locations where data was obtained, rather than only 4 selected locations

Response 5:

The inlet flow conditions and operating temperature for the MARIGNAN tests are provided in Table Q5-1.

Table Q5-1: Inlet and Operating Conditions for the MARIGNAN Test

[ ]

Section 5.2.2 provides a general description of the test configuration. The COBRA-FLX geometry model was comprised of a total of 496 subchannels by the 16x31 subchannel array. Figure 5-9 displays the boundaries of the individual subchannels modeled where the interface (Row Identifier = 0) between the two fuel assemblies intersects the shared subchannels between the fuel assemblies. The axial noding used in the COBRA-FLX simulation was 11mm. The spacer grid hydraulic resistance was simulated by individual subchannel loss coefficients for the various types of subchannels contained in the configuration. A diversion cross flow resistance factor, K_{ij}, of 0.15 was used for the simulation.

The measured data from the MARIGNAN test, using Laser Doppler Velocimetry (LDV) techniques, were entrained particle velocities in the axial and transverse flow. The measured particle velocity data within the subchannels were reduced to average axial velocities within each subchannel to yield experiment based results. Therefore, the phrase "MARIGNAN Measurements" in the plots and text actually represents reduced measured data.

As discussed and agreed upon during the RAI Clarification Conference Call, the comparison of COBRA-FLX predictions is given versus reduced measured data, in this case a normalized axial velocity of V/V_{mean}, as this is the basic information currently available to AREVA. The V/V_{mean} is defined in Equation 5-5 in Section 5.2.2 and is based upon a V_{mean} of 4.8 m/s. All data for 21 axial elevations and the 9 rows at the bundle interfaces (in total 189 data points) is provided in the following Figures Q5-1 through Figures Q5-21. These figures provide the COBRA-FLX predictions using both the P, in this case P using [ ] SOR, and the PV solution methods together with the reduced measured data. Figure Q5-10 represents the condition immediately upstream of the axial plane containing the mid-span mixing grid (see Figure 5-10 for the specific mid-span mixing grid). Figure Q5-11 represents the condition immediately downstream of the mid-span mixing grid. The range of test conditions were limited to the specific test conditions in Table Q5-1.

Figure Q5- 1: Axial Velocity Comparisons by Subchannel Row at the Relative Axial Location of Y= - 200 mm in the MARIGNAN Test

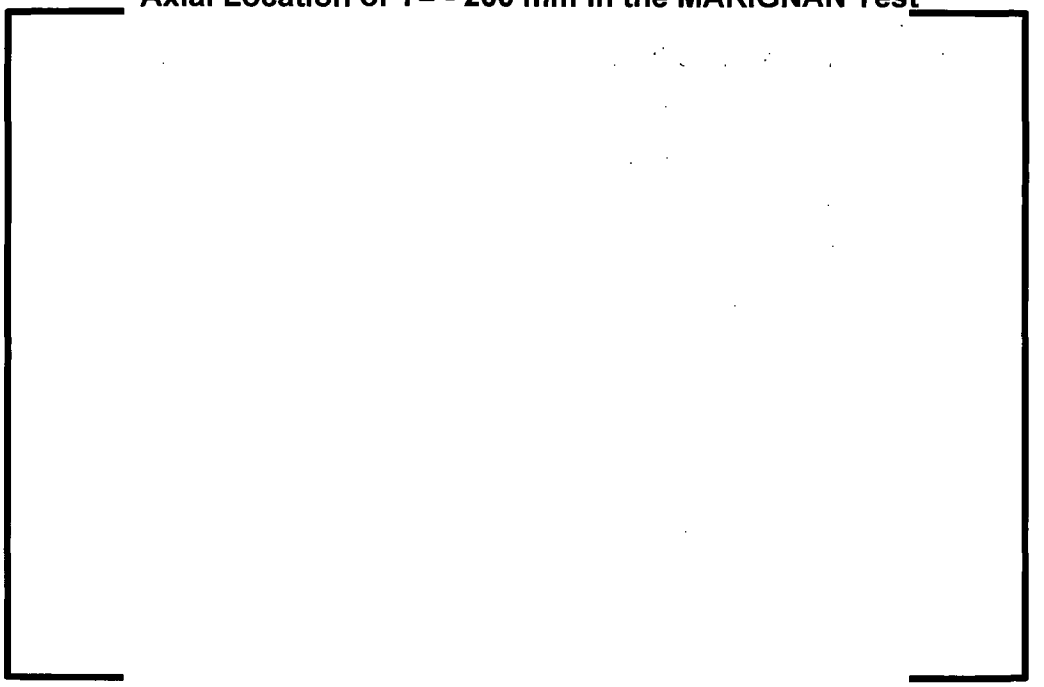

Figure Q5- 2: Axial Velocity Comparisons by Subchannel Row at the Relative Axial Location of Y= - 180 mm in the MARIGNAN Test

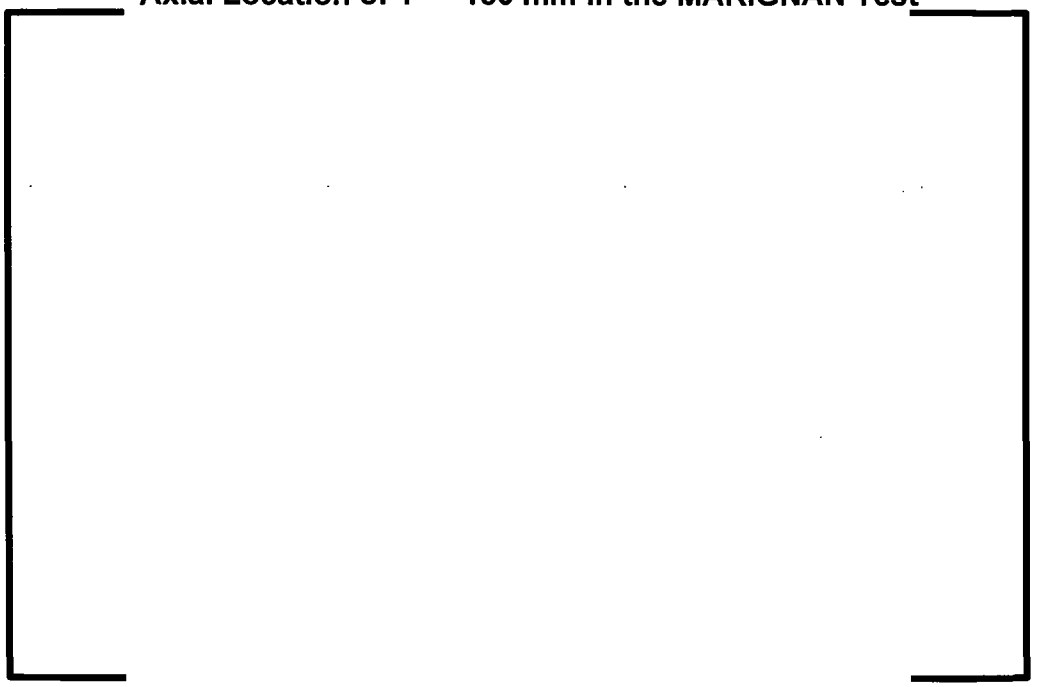

Figure Q5- 3: Axial Velocity Comparisons by Subchannel Row at the Relative Axial Location of Y= - 160 mm in the MARIGNAN Test

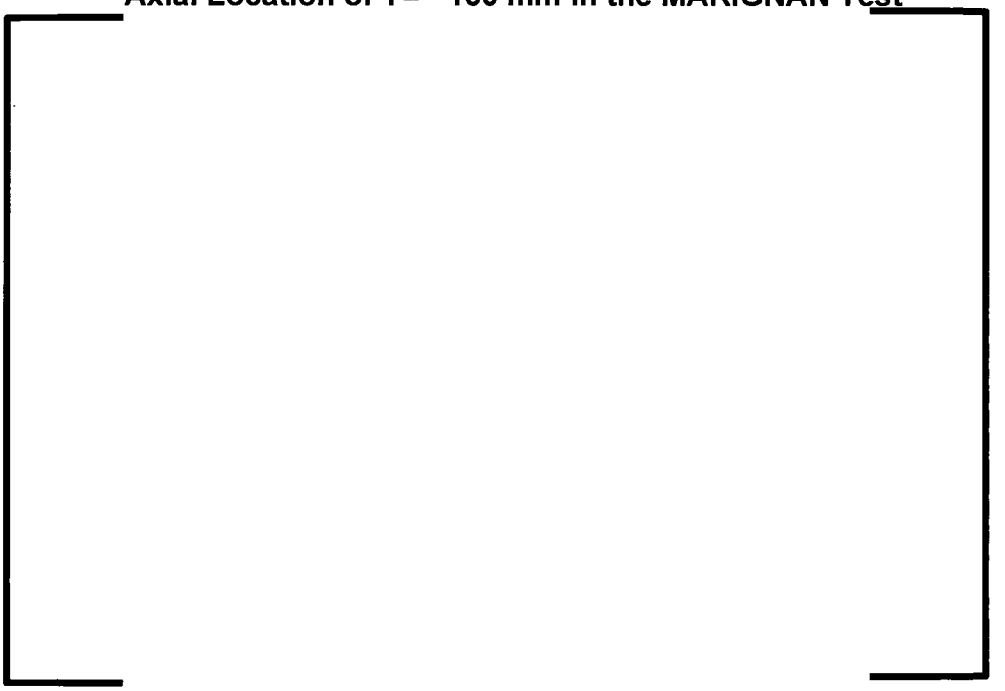

Figure Q5- 4: Axial Velocity Comparisons by Subchannel Row at the Relative Axial Location of Y= - 140 mm in the MARIGNAN Test

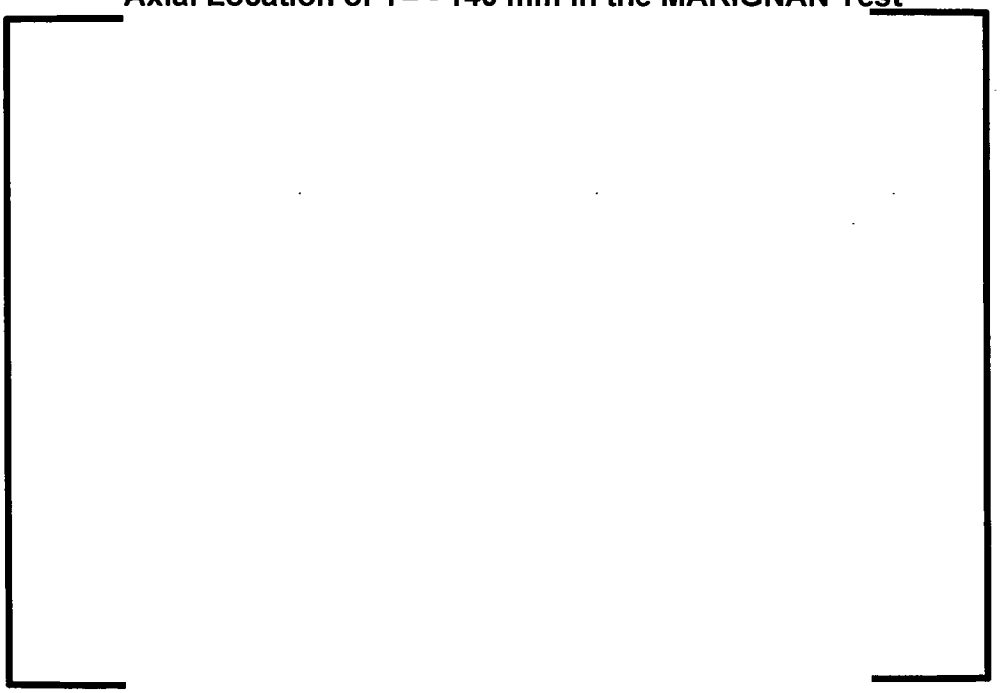

Figure Q5- 5: Axial Velocity Comparisons by Subchannel Row at the Relative Axial Location of Y= - 100 mm in the MARIGNAN Test

Figure Q5- 6: Axial Velocity Comparisons by Subchannel Row at the Relative Axial Location of Y= - 80 mm in the MARIGNAN Test

Figure Q5- 7: Axial Velocity Comparisons by Subchannel Row at the Relative Axial Location of Y= - 60 mm in the MARIGNAN Test

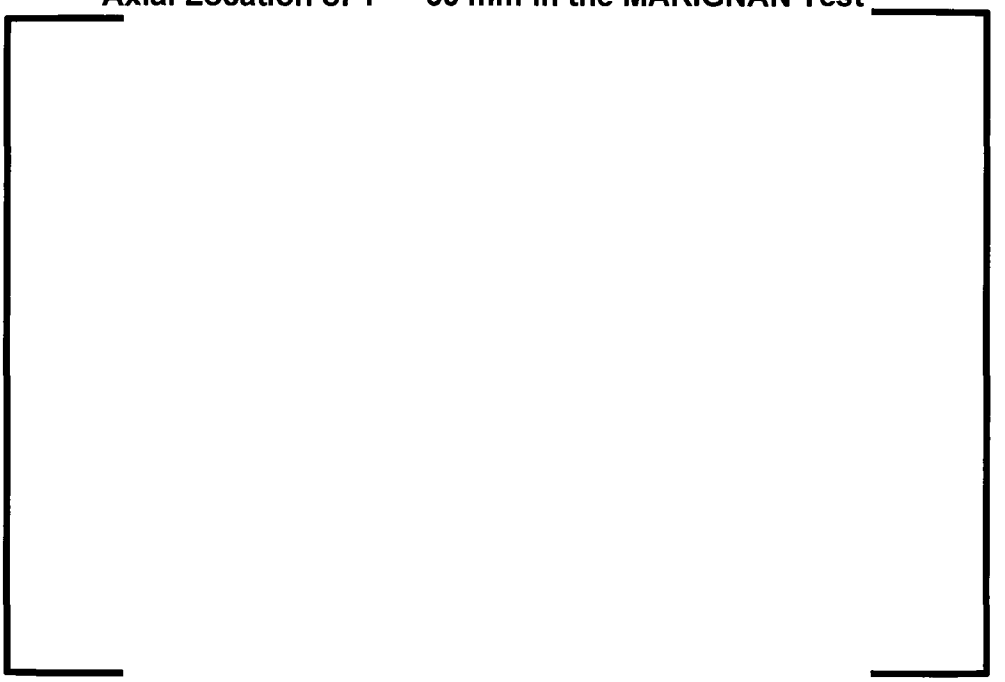

Figure Q5- 8: Axial Velocity Comparisons by Subchannel Row at the Relative Axial Location of Y= - 40 mm in the MARIGNAN Test

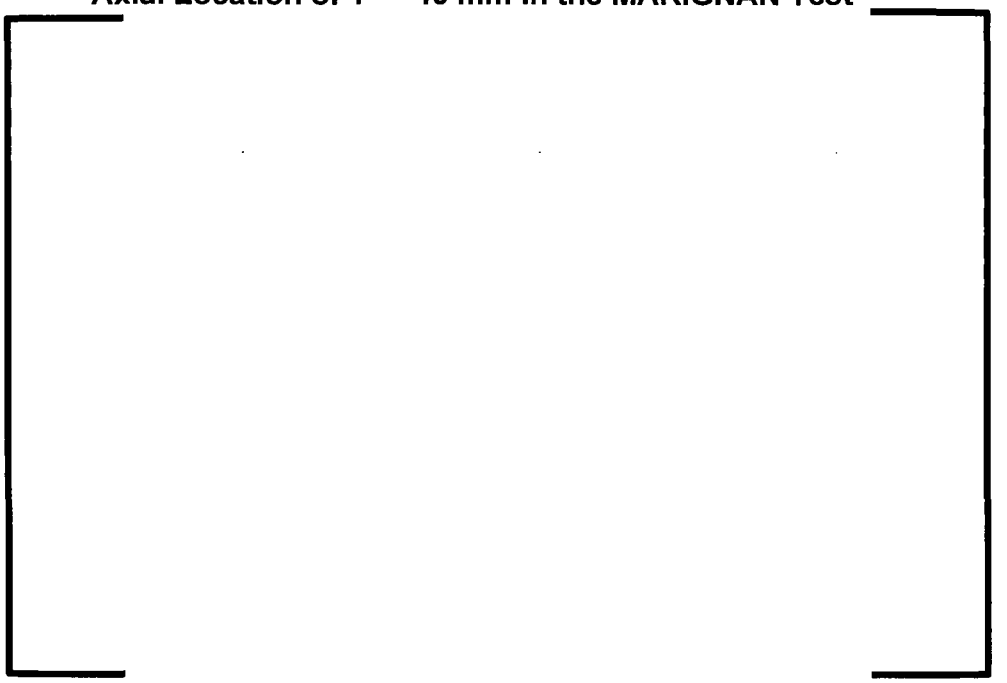

Figure Q5- 9: Axial Velocity Comparisons by Subchannel Row at the Relative Axial Location of Y= - 20 mm in the MARIGNAN Test

Figure Q5- 10: Axial Velocity Comparisons by Subchannel Row at the Relative Axial Location of Y= - 7.5 mm in the MARIGNAN Test

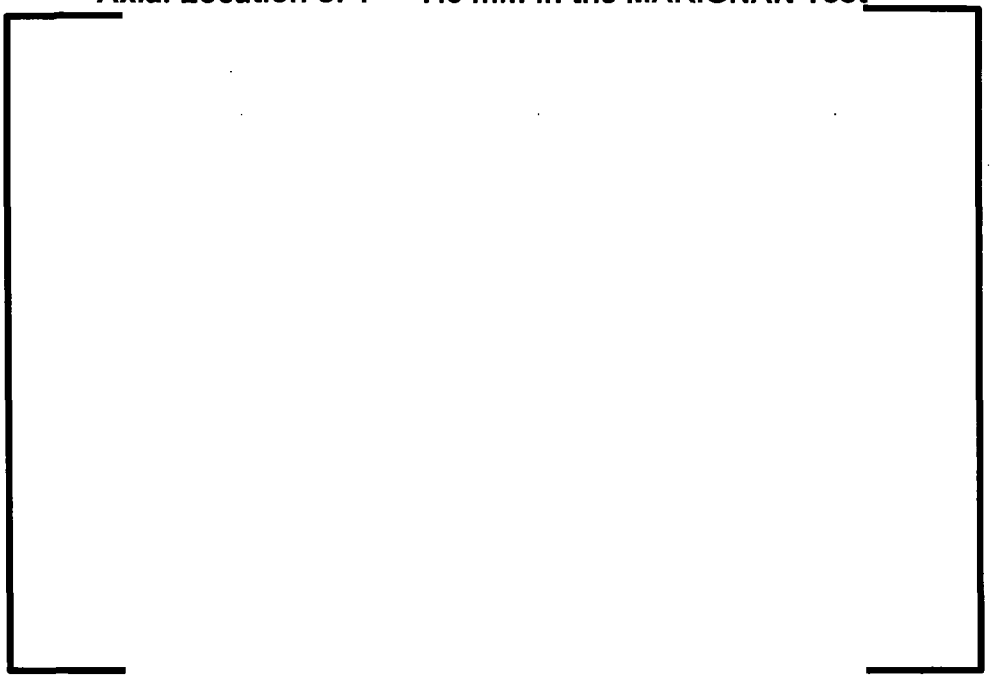

Figure Q5- 11: Axial Velocity Comparisons by Subchannel Row at the Relative Axial Location of Y= 7 mm in the MARIGNAN Test

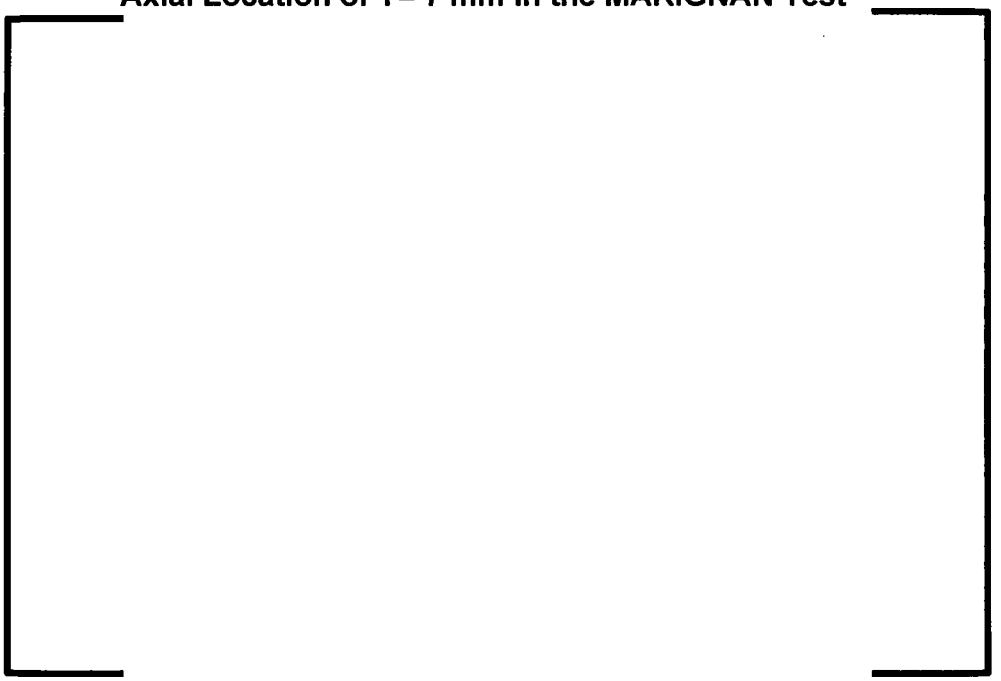

Figure Q5- 12: Axial Velocity Comparisons by Subchannel Row at the Relative Axial Location of Y= 20 mm in the MARIGNAN Test

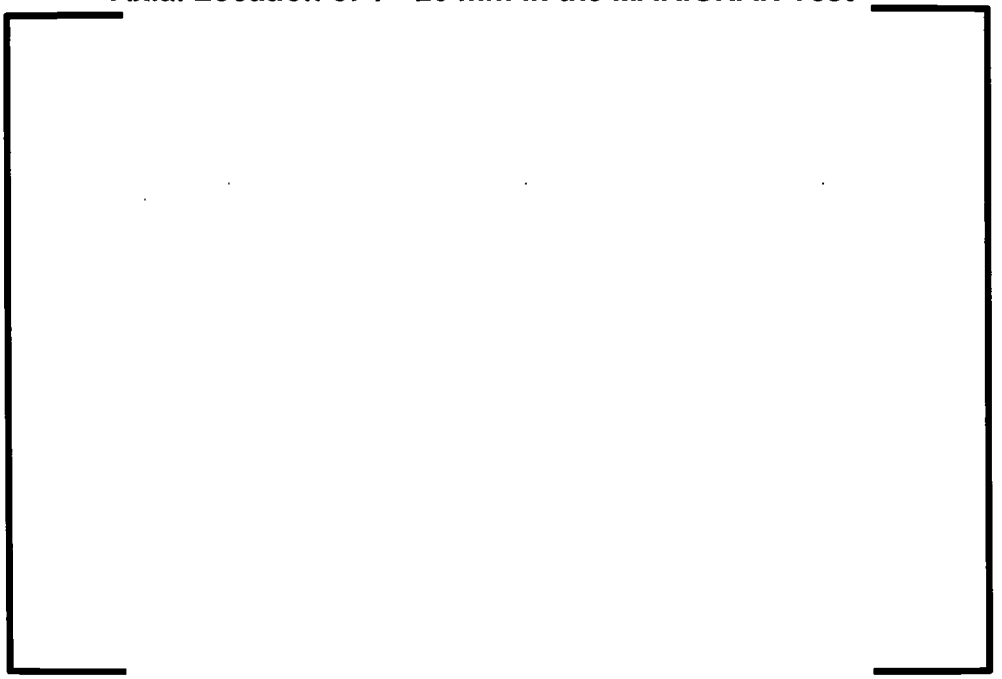

Figure Q5- 13: Axial Velocity Comparisons by Subchannel Row at the Relative Axial Location of Y= 40 mm in the MARIGNAN Test

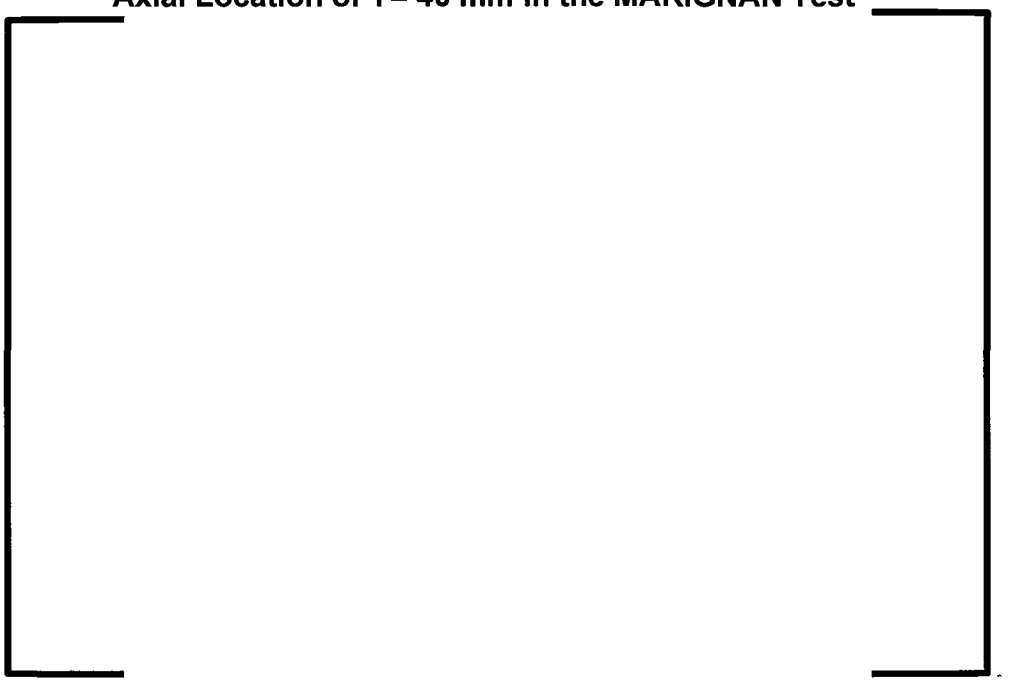

Figure Q5- 14: Axial Velocity Comparisons by Subchannel Row at the Relative Axial Location of Y= 60 mm in the MARIGNAN Test

Figure Q5- 15: Axial Velocity Comparisons by Subchannel Row at the Relative Axial Location of Y= 80 mm in the MARIGNAN Test

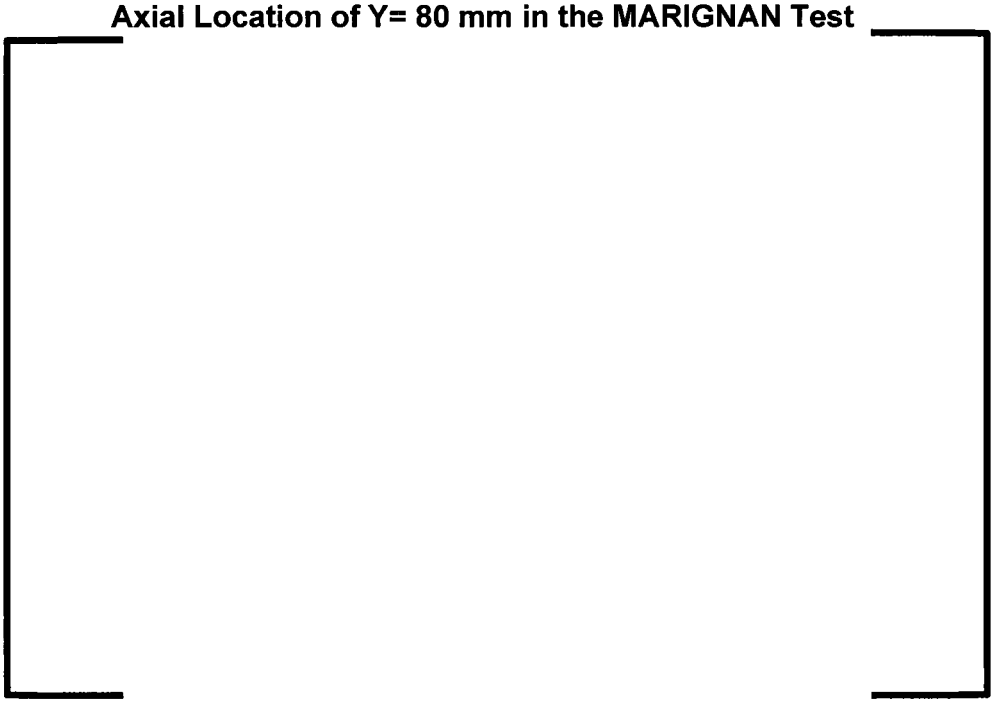

Figure Q5- 16: Axial Velocity Comparisons by Subchannel Row at the Relative Axial Location of Y= 90 mm in the MARIGNAN Test

Figure Q5- 17: Axial Velocity Comparisons by Subchannel Row at the Relative Axial Location of Y= 130 mm in the MARIGNAN Test

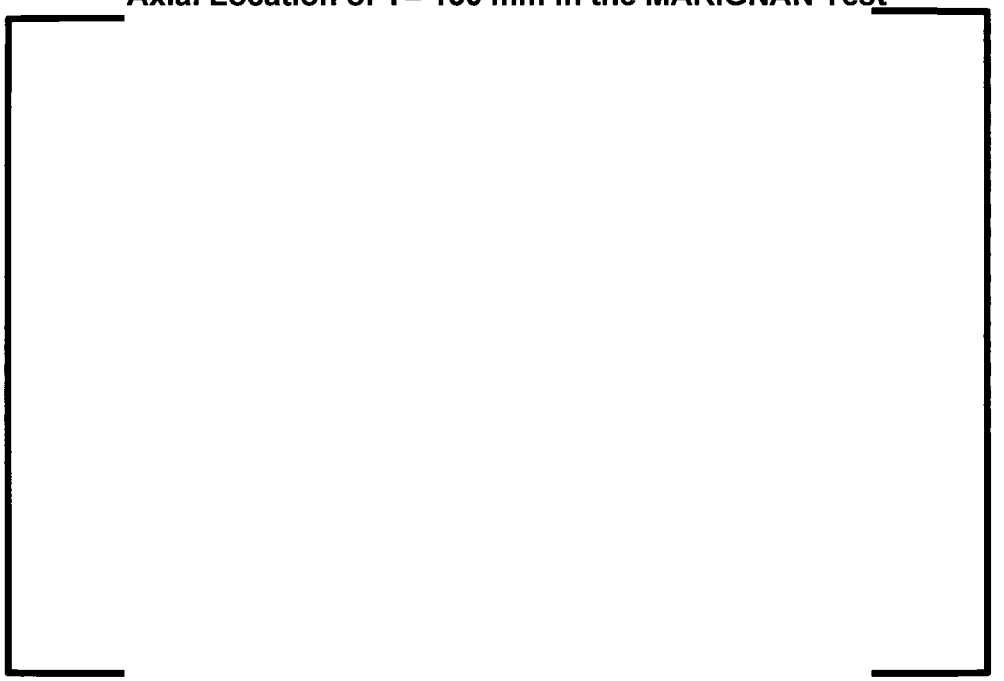

Figure Q5- 18: Axial Velocity Comparisons by Subchannel Row at the Relative Axial Location of Y= 140 mm in the MARIGNAN Test

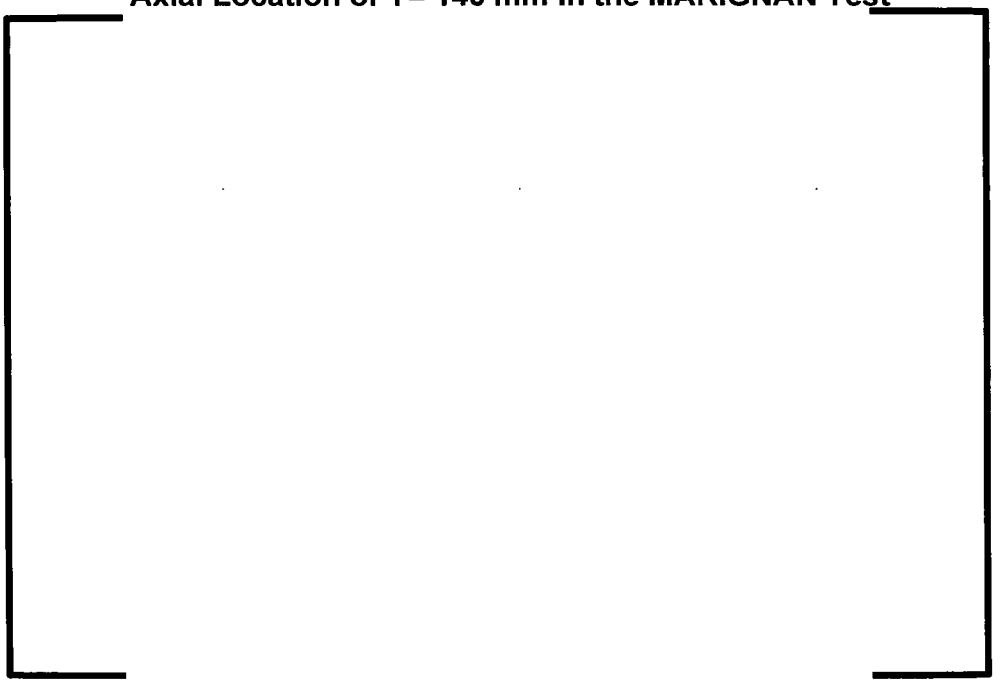

Figure Q5- 19: Axial Velocity Comparisons by Subchannel Row at the Relative Axial Location of Y= 160 mm in the MARIGNAN Test

Figure Q5- 20: Axial Velocity Comparisons by Subchannel Row at the Relative Axial Location of Y= 180 mm in the MARIGNAN Test

Figure Q5- 21: Axial Velocity Comparisons by Subchannel Row at the Relative Axial Location of Y= 200 mm in the MARIGNAN Test

Request 6:

(Validation of Solution Methods) Section 5.2.2, p. 5-16: The document states that in comparison to the MARIGNON test data, "The COBRA-FLX axial velocity predictions were found to be within 5% of the measured values for 90% of the data." This is an insufficient description of the results of the validation of the COBRA-FLX solution methods with this data set.

a. What is the basis for the 5% and 90% values given?

b. What are the characteristics of the 10% of the data where the COBRA-FLX predictions are not within 5% of the measured values?

Response 6:

The following Figure Q6-1 presents the statistical comparison of the MARIGNAN reduced measurement data against the COBRA-FLX predictions with the P solution and [ ]. A total of 189 data points (9 rows at 21 axial levels) are available. The overall agreement between COBRA-FLX predictions and the reduced measurement data is good, as 171 of the data points (more than 90%) do not differ more than ±5%. The remaining 18 data points (less than 10%) do not differ more than ±10% in the results. A majority of the predictions more than ±10% of the reduced measurement data are associated with predictions well upstream (e.g., where Y= -200 mm to -140 mm) of the MSMG plane near the bundle interface. This can be more easily appreciated by examining the differences between COBRA-FLX prediction and the reduced measured data in Figures Q5-1 through Q5-4. COBRA-FLX predictions at and downstream of the axial plane of the MSMG agree well with the reduced measured data.

In addition, COBRA-FLX predictions with the PV solution have been generated and compared to the reduced measured data in Figure Q6-2. The comparison of these two figures indicates that both solution methods give nearly identical results, where all deviations between both solutions are well below 1% (standard deviation 0.0036).

Figure Q6- 1: Comparison of Measured and Predicted Relative Velocities in Rows of Channels using the P Solution (with [ ])

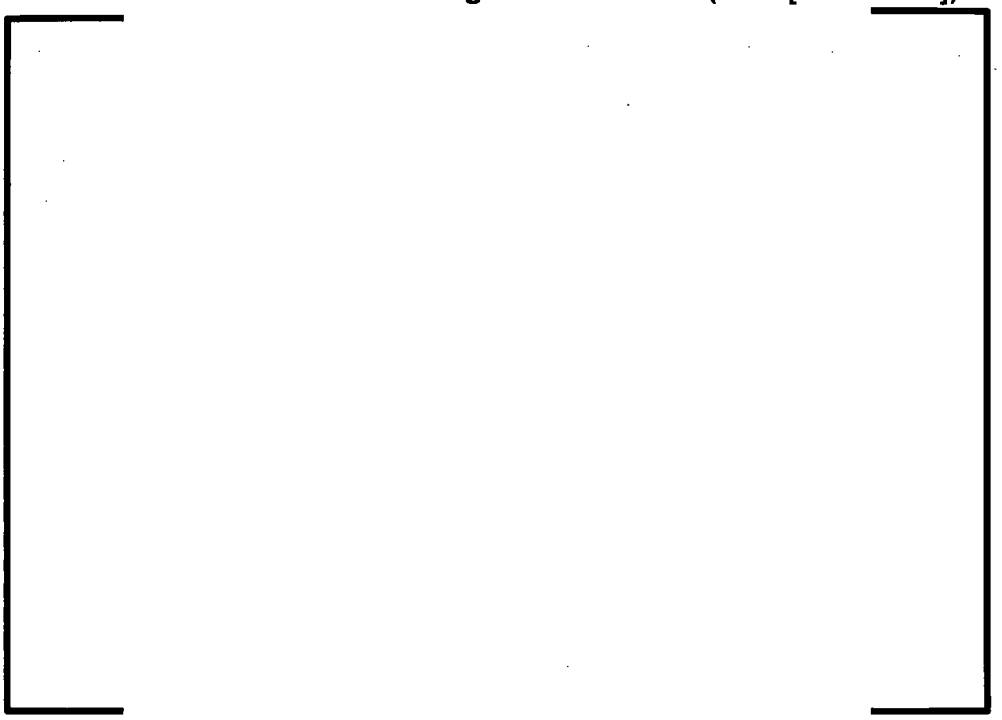

Figure Q6- 2: Comparison of Measured and Predicted Relative Velocities in Rows of Channels using the PV Solution

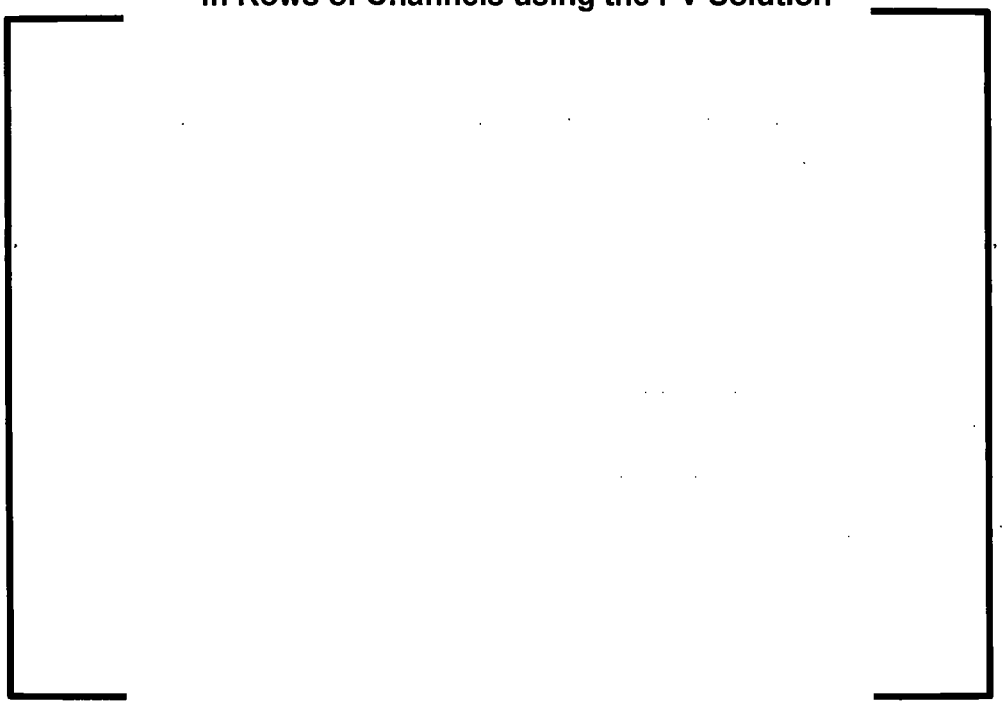

Request 7:

(Validation of Solution Methods) The documentation of the COBRA-FLX mathematical modeling and solution algorithms does not discuss the potential limitations of using a profile-fit void/quality model in transient two-phase flow calculations. In the discussion of the mathematical model, this issue is dismissed on p. 2-20 with the statement that the two-phase flow structure is "fine enough" to allow void fraction to be specified "as a function of enthalpy, pressure, coolant flow rate, axial position, and time". Due to simplifications inherent in the continuity equations where two-phase flow is treated as a homogeneous mixture, the solution can become unstable or converge to a physically incorrect solution in transient calculations. This behavior is caused by physically unrealistic instantaneous changes in void with local conditions, due to calculating the relationship between void and quality based on a profile fit derived from steady-state data. How is this limitation in the 3-equation mixture model addressed in the COBRA-FLX code solution methods and applications?

Response 7:

The profile-fit void/quality models used in many of the current generation subchannel codes were originally developed for steady-state applications but are applied for transient analyses. Examples of the subchannel codes using this assumption include COBRA-FLX, LYNXT (Reference 5-1), and VIPRE-01 (Reference Q-J). The same profile-fit modeling is also used in the parents for COBRA-FLX (COBRA-IIIC/MIT (Reference Q-K)) and LYNXT (COBRA-IV (Reference Q-L)). Thus, the transient stability issue is not limited to COBRA-FLX.

The subcooled boiling and bulk void models of COBRA-FLX calculate void fractions as a function of quality, as well as mass flux. In a transient, a small change in the flow can yield a change in the void fraction that is quite independent of any consideration of how that vapor could be transported or generated. This can be accompanied by physically unrealistic instantaneous changes in void based on the calculated local conditions. Based on AREVA's approximately 25 years of licensing experience with COBRA-3CP (AREVA internal parent code for COBRA-FLX which is based on COBRA-IIIC/MIT) and approximately 30 years of licensing experience with LYNXT, this issue has not been observed for standard PWR applications.

AREVA will address this potential code convergence/stability issue by modifying the COBRA-FLX user guidelines to describe how to identify and address the potential transient instabilities due to the profile-fit void/quality model.

Request 8:

(Validation of Model Components) Section 5.3, p. 5-19 states that empirical correlations included in Table 1-2 have been used with the COBRA 3-CP code, and therefore "no experimental validation is being presented for these empirical correlations." However, the Chexal-Lellouche bulk void model, as implemented in COBRA-FLX, is not consistent with the model as described in the primary reference[1]. In COBRA-FLX, the two-phase flow model consists of three separate components; the void correlation, the correlation for the initiation of subcooled void formation, and the profile-fit correlation relating local quality and void fraction. The specific correlations under review for the two-phase flow model are Chexal-Lellouche (for the void correlation), Saha-Zuber (for the initiation of subcooled void), and Zuber-Staub (for the profile-fit correlation). Saha-Zuber and Zuber-Staub are not the models presented in the primary reference for these components of the Chexal-Lellouche model. Justify the use of Saha-Zuber and Zuber-Staub for these components of the Chexal-Lellouche model

a. by comparison to the models for these components that are documented in the primary reference

b. by comparison to relevant experimental data from the primary reference, showing that the void initiation point and the profile-fit obtained with Saha-Zuber and Zuber-Staub, respectively, produce comparable results to those obtained with the primary model

Response 8:

As discussed and agreed upon during the RAI Clarification Conference Call, the use of the Saha-Zuber and Zuber-Staub models together with the Chexal-Lellouche void correlation is being justified by comparison to measurement data which is available to AREVA. This includes two parts: 1) comparison to steady-state measurement data obtained at AREVA's thermal-hydraulic test loop KATHY, and 2) analysis of the NUPEC transient boiling experiments for a single channel.

---

[1] The primary reference for the Chexal-Lellouche model in the COBRA-FLX document is Reference A-12, B. Chexal, G. Lellouche, J. Horowitz, and J. Healzer, *A Void Fraction Correlation for Generalized Applications*, **Progress in Nuclear Energy**, Vol. 27, No. 4, 1992.

1) Comparison to steady-state measurement data

The void measurements for the BWR fuel design ATRIUM 10XM have been performed at AREVA's thermal-hydraulic test loop KATHY at Karlstein, Germany in 2009. A description of the test loop and the methodology to obtain void data is published by Wehle et al. (2010) in Reference Q-G. The data have also been used to verify the US NRC approved computer codes XCOBRA, MICROBURN-B2, S-RELAP5 and RAMONA5-FA. It should be mentioned here that, for example, RAMONA5-FA is also using the Chexal-Lellouche bulk-void correlation together with different models than the primary reference in the sub-cooled region.

The tests were performed using down-skew power profiles, with a range of [

]. A total of [ ] measurement data points were analyzed using the COBRA-FLX computer code simulating the test bundle. In these calculations the models Chexal-Lellouche (for the bulk void correlation), Saha-Zuber (for the initiation of sub-cooled void), and Zuber-Staub (for the profile-fit correlation) have been used. The comparison is based on measured planar bundle average void fractions. The results are illustrated in Figure Q8-1 below.

Figure Q8-1: COBRA-FLX Predicted Versus Steady-State Measured Void Fractions

The overall comparison shows a very good agreement between predicted and measured values over the entire range of void fractions. Nearly all of the data fall within the error band of [ ] indicating the measurement uncertainty.

In Table Q8-1 a statistical evaluation of the [ ] measurement data points is given. The obtained mean value, as well as the standard deviation, is in the same range as known from comparisons with other thermal-hydraulic codes.

Table Q8-1: Statistics of COBRA-FLX (calculated – measured void fraction) Regarding the Recalculated Steady-State Void Measurements

2) Comparison to Transient Experiments

As documented in Kolev (2006), Reference Q-H, and the references given within (Hori et al. (1994), Reference Q-I), there exist transient experiments on a heated channel with a 1.5 m length representing a single internal sub-channel of a PWR fuel assembly. The measured value is the mixture density at the exit of the channel as a function of time. In total four transient measurements have been performed, each with one of the boundary conditions varying in time. The initial conditions for the four test cases are summarized in Table Q8-2.

Table Q8-2: Initial Conditions for the Four Transients

No.	Power [kW]	Inlet Temperature [°C]	Pressure [bar]	Mass flow rate x10^6 [kg/(m²h)]
Case1	55	315	155	12
Case2	55	315	155	12
Case3	55	315	155	12
Case4	75	305	155	12

In the following four figures Q8-2, Q8-3, Q8-4, and Q8-5, for each test case the transient varied parameter (forcing function) is given. These forcing functions are also applied to a COBRA-FLX calculation simulating the experiment. Again, in these calculations the models Chexal-Lellouche (for the bulk void correlation), Saha-Zuber (for the initiation of sub-cooled void), and Zuber-Staub (for the profile-fit correlation) have been used.

Figure Q8-2: Forcing Function of the Inlet Velocity for Case 1

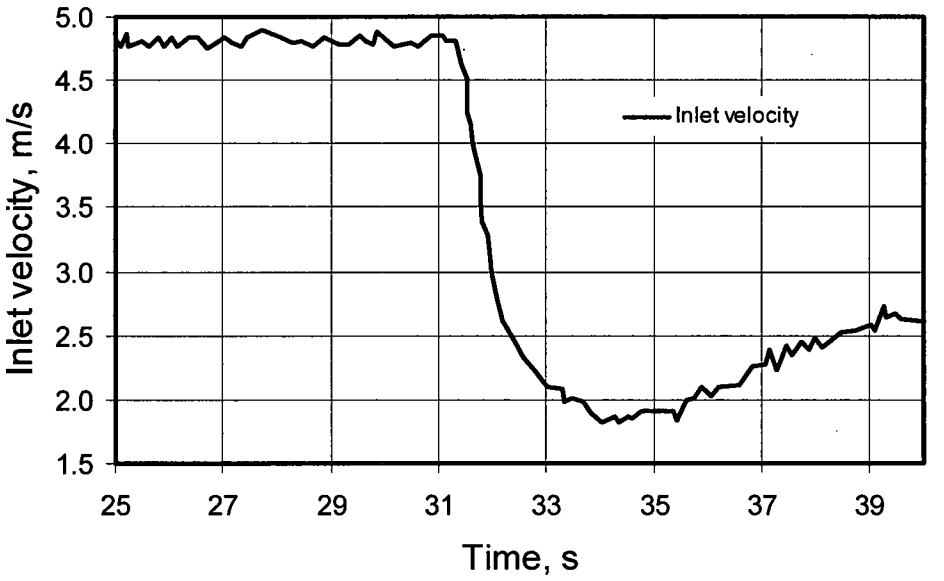

Figure Q8-3: Forcing Function of the Inlet Velocity for Case 2

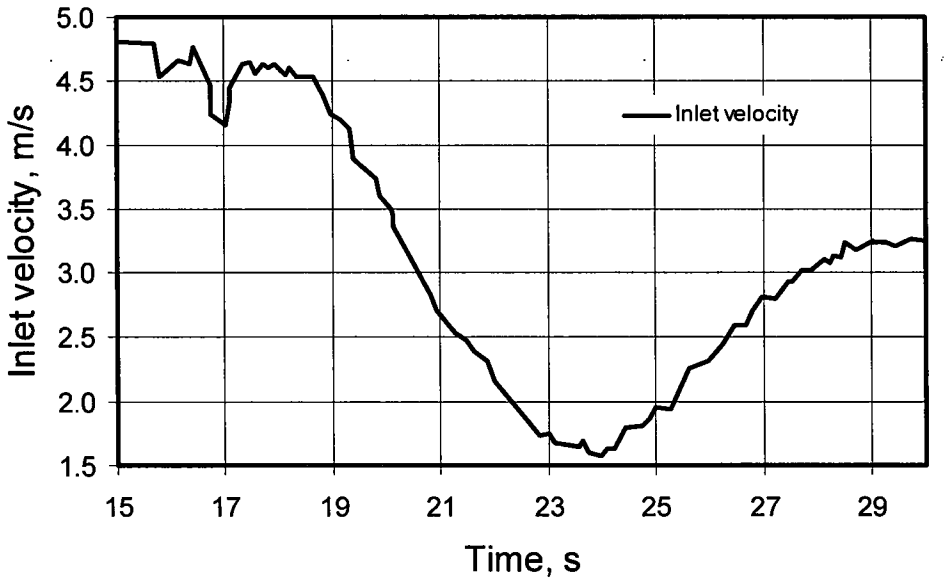

Figure Q8- 4: Forcing Function of the System Pressure for Case 3

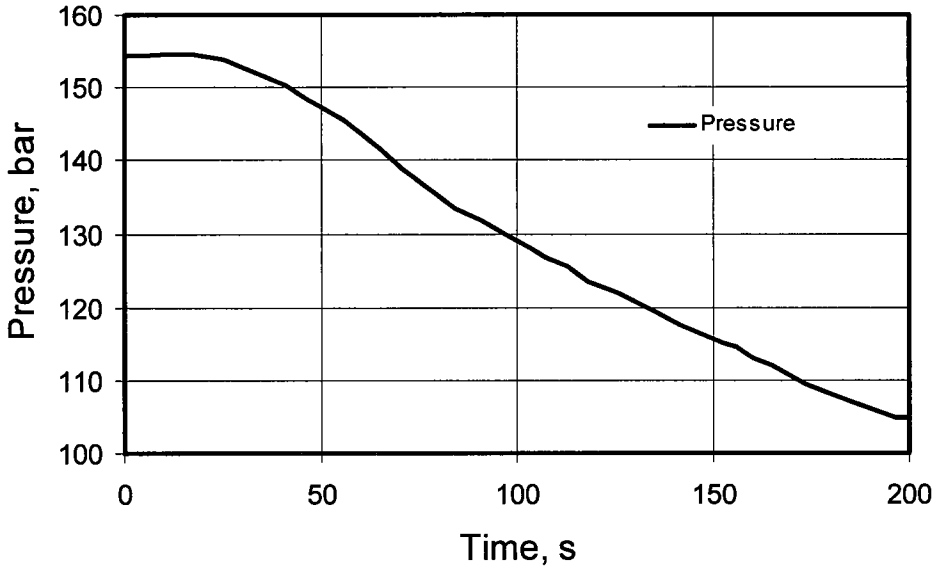

Figure Q8- 5: Forcing Function of the Inlet Water Temperature for Case 4

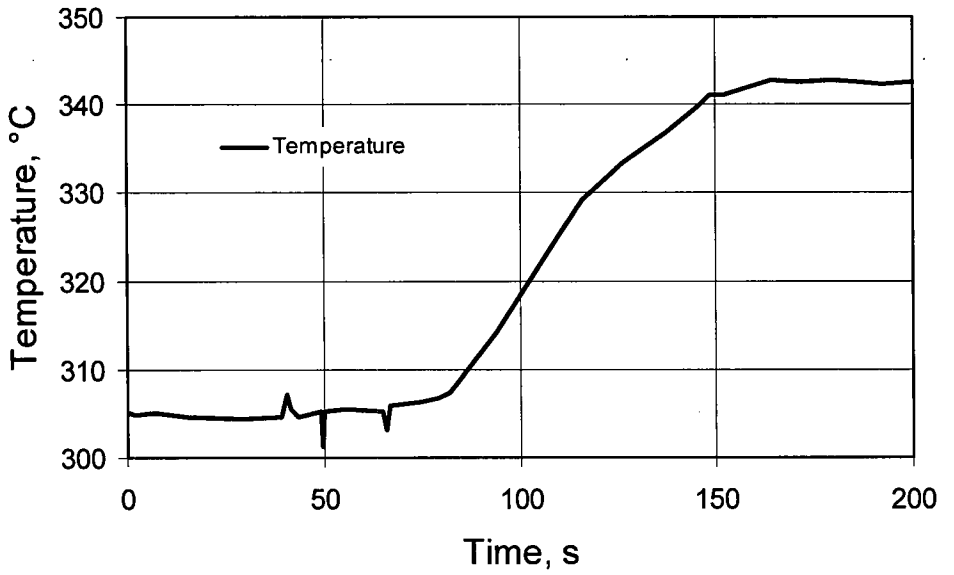

The comparison of measured and calculated results is based on the mixture density as illustrated in Figures Q8-6, Q8-7, Q8-8 and Q8-9.

Figure Q8- 6: Comparison of Measured and Computed Mixture Density for Case 1

Figure Q8- 7: Comparison of Measured and Computed Mixture Density for Case 2

Figure Q8- 8: Comparison of Measured and Computed Mixture Density for Case 3

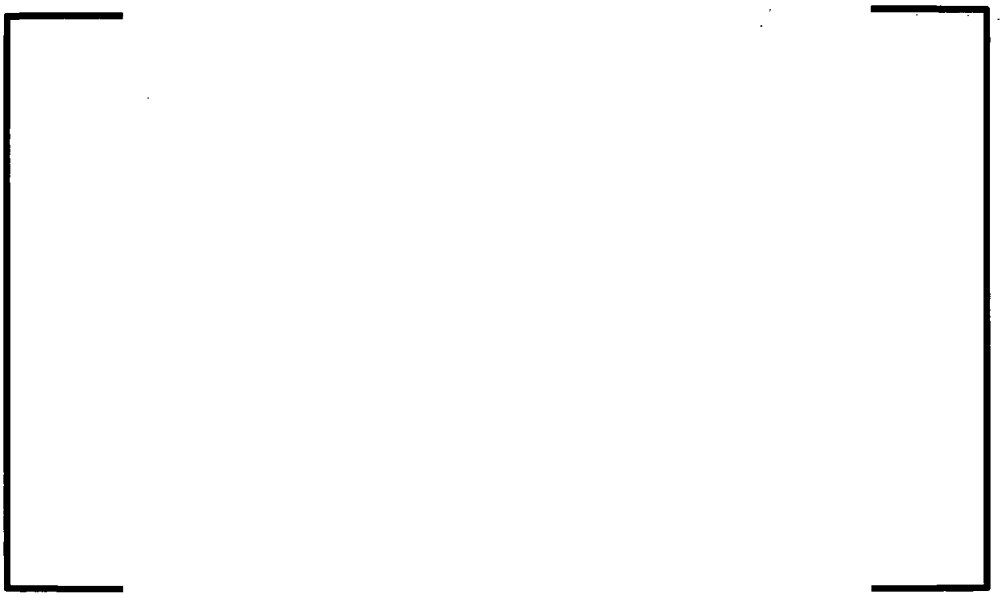

Figure Q8- 9: Comparison of Measured and Computed Mixture Density for Case 4

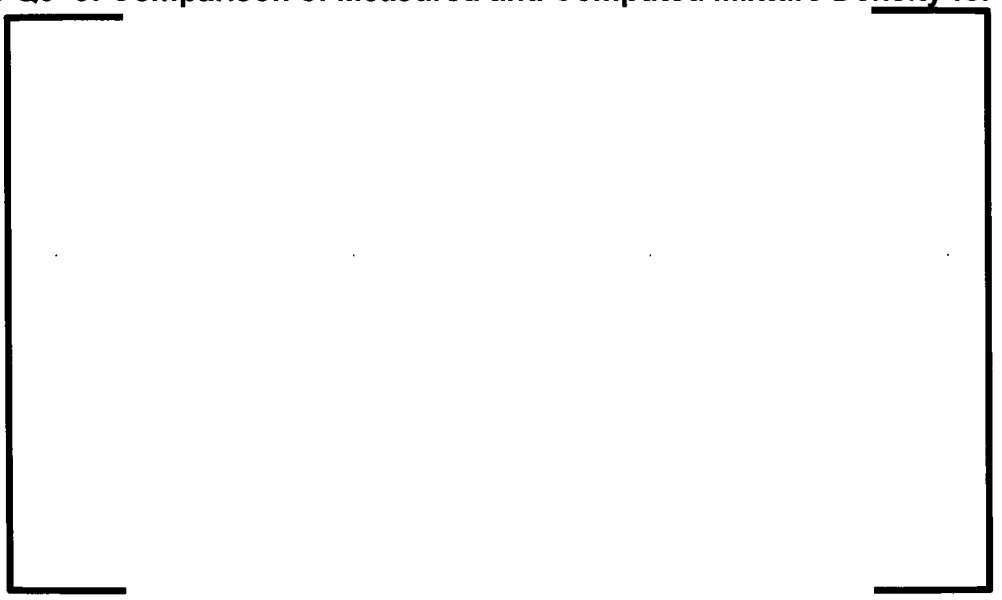

As it can be seen, COBRA-FLX gives quite reasonable results and the agreement between calculation and experiment can be considered as good.

As a result of both, the comparison to steady-state measurement data obtained at AREVA's thermal-hydraulic test loop KATHY as well as to the NUPEC transient boiling experiments, the combination of the models Chexal-Lellouche (for the bulk void correlation), Saha-Zuber (for the initiation of sub-cooled void), and Zuber-Staub (for the profile-fit correlation) is justified.

Request 9:

(Validation of Model Components) Section A.3.2.1 *Homogeneous Model*: The homogeneous two-phase flow friction multiplier, as documented in the COBRA-FLX report (p. A-5) is incomplete and appears incorrect. For this evaluation to be complete, this item must be addressed by

a. verifying or correcting the correlation as documented in the code

b. verifying that the implementation of the correlation in the code is correct

Response 9:

The equation for the homogenous two-phase friction multiplier, as given in the COBRA-FLX topical report, is correct but needs some more explanation which is provided here. In response to Part (a), the two-phase friction pressure loss is commonly (e.g. Reference Q-C), Section 5.4.1) correlated in terms of dynamic head:

$$\Delta p_{2\Phi} = K \frac{G^2}{2\rho_{2\Phi}}$$

G is the mass flux, K is an empirical irreversible loss coefficient and $\rho_{2\Phi}$ is an appropriate two-phase density.

For the limiting case of saturated, homogeneous two-phase flow $\rho_{2\Phi}$ equals the homogeneous density ρ_H, which results in

$$\Delta p_{2\Phi} = K \frac{G^2}{2\rho_f}\left(\frac{\rho_f}{\rho_H}\right)$$

After renaming ρ_H to $\rho_{mixture}$ and denoting the two-phase friction multiplier to the single-phase pressure loss by Φ one obtains

$$\Phi = \frac{\rho_f}{\rho_H} = \frac{\rho_f}{\rho_{mixture}}$$

which is the definition as given in the topical report on page A-5.

Since $\rho_{mixture} = \rho_H$ and the homogeneous density ρ_H is defined by

$$\rho_H = \frac{1}{v_f + x \cdot v_{fg}} = \frac{1}{\frac{1}{\rho_f} + x\frac{\rho_f - \rho_g}{\rho_f \cdot \rho_g}} = \frac{\rho_f}{1 + x\left(\frac{\rho_f}{\rho_g} - 1\right)}$$

the homogeneous two-phase flow friction multiplier is

$$\Phi = 1 + x\left(\frac{\rho_f}{\rho_g} - 1\right)$$

which is the most commonly known formulation.

In response to Part (b), the sequence of calculations in COBRA-FLX is as follows:

1. First, the void fraction α for homogeneous flow is calculated.

$$\alpha = \frac{x}{(1-x)\frac{\rho_g}{\rho_f} + x}$$

2. Secondly, the $\rho_{mixture}$ is calculated.

$$\rho_{mixture} = \rho_g \alpha + \rho_f (1 - \alpha)$$

3. Lastly, the two-phase flow friction multiplier is calculated:

$$\Phi = \frac{\rho_f}{\rho_{mixture}}$$

which is equivalent to

$$\Phi = 1 + x\left(\frac{\rho_f}{\rho_g} - 1\right)$$

By these more detailed explanations is verified that the definition of the homogenous two-phase flow friction multiplier, as used in COBRA-FLX, is correct. The implementation of the multiplier has been verified in the course of code certification.

Request 10:

(Validation of Model Components) Section A.5 *Heat Transfer Coefficients*: The heat transfer package to be used in licensing application of the COBRA-FLX code is incompletely documented. For this evaluation to be complete, the following items must be addressed;

a. justify the use of the Sieder-Tate heat transfer correlation (p. A-28) for single phase liquid forced convection applications; this correlation was derived as a modification to the Dittus-Boelter heat transfer correlation for high-temperature gas flows.

b. justify the use of the McAdams heat transfer correlation (p. A-28) for single phase liquid forced convection applications; the formulation provided in the documentation is for natural convection in air.

c. define explicitly and justify the heat transfer correlations that will be used in post-CHF heat transfer calculations in licensing or safety-related applications with COBRA-FLX. The documentation in Section A.5 on this is application is unclear and incomplete.

Response 10:

Both heat transfer correlations for use in turbulent conduit flow, the Dittus-Boelter correlation and the Sieder-Tate correlation, belong to the "Nusselt form"

$$Nu = c\,\mathrm{Re}^{m}\,\mathrm{Pr}^{n}$$

$$Nu = \frac{hD_e}{k_i}$$

Perhaps the most widely quoted and used heat transfer correlation for fully developed turbulent heat transfer to single phase liquid (index *i* refers to subcooled liquid or superheated steam) is that of Dittus-Boelter in Reference Q-C.

$$h_{DB} = 0.023\frac{k_i}{D_e}\mathrm{Re}_i^{0.8}\,\mathrm{Pr}_i^{n}$$

with $n = 0.4$ for heating $(T_{wall} > T_b)$ and $n = 0.3$ for cooling $(T_{wall} < T_b)$. It is applicable for $\mathrm{Re} > 10{,}000$ and $0.7 \le \mathrm{Pr} \le 160$. It is recommended for moderate temperature differences, $T_{wall} - T_b$, as stated in Reference Q-C.

The Sieder-Tate correlation in Reference Q-D, as given in Reference Q-E, looks as a modified version of the Dittus-Boelter correlation:

$$h_{ST} = 0.023 \frac{k_i}{D_e} \mathrm{Re}_i^{0.8} \mathrm{Pr}_i^{0.33} \left(\frac{\mu_i}{\mu_{wall}} \right)^{0.14}$$

This correlation is based on experimental data for water, kerosene, benzene and a variety of different oils. It is applicable for $\mathrm{Re} > 10{,}000$ and $0.7 \le \mathrm{Pr} \le 16{,}700$. The important improvement is the viscosity term

$$\left(\frac{\mu_i}{\mu_{wall}} \right)^{0.14},$$

which allows its usage for large temperature differences $T_{wall} - T_b$. Therefore the Sieder-Tate correlation provides a wider range of applicability.

For typical PWR usage the difference between the Dittus-Boelter correlation and the Sieder-Tate correlation is small. This is illustrated in Figure Q10-1 which is based on boundary conditions of water, pressure of 160 bar, temperature of 300 °C, and heat flux of 1.2E+06*(Re/4.692E+05) W/m^2.

Figure Q10-1: COBRA-FLX: Comparison of Heat Transfer Correlations, Sieder-Tate and Dittus-Boelter

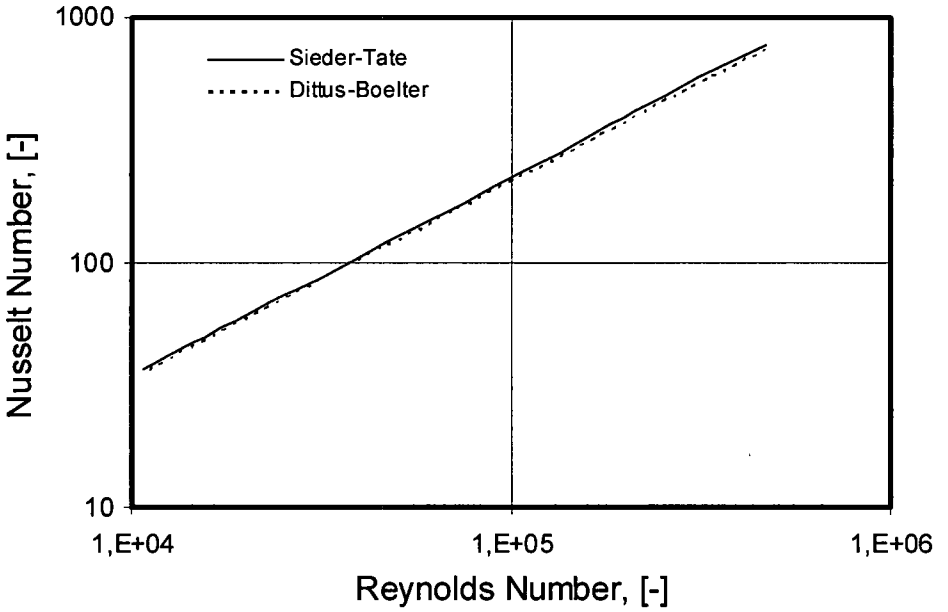

Figure Q10-1 is based upon the heat flux being set directly proportional to the Reynolds Number in order to keep the power-to-flow ratio constant. The Nusselt Number calculated with the Sieder-Tate correlations are 2% to 4% larger than the values calculated with the Dittus-Boelter correlation for Reynolds Numbers from 10,000 to 470,000.

Based on this comparison, the Sieder-Tate heat transfer correlation is justified for use in typical COBRA-FLX applications.

For very low flows, natural convection may become a significant contributor to the total heat transfer. Natural convection is modeled by the correlation of McAdams in Reference Q-F, which is based on data for heating water in vertical pipes and recommended for upward flow past vertical surfaces:

$$h_{MA} = 0.13 k_i \left[\frac{\rho_i^2 g \beta_i c_{p,i} (T_{wall} - T_v)}{\mu_i k_i} \right]^{(1/3)}$$

which can also be written in the following "Nusselt form" as function of the Grashof Number Gr and the Prandtl Number Pr.

$$Nu_{MA} = 0.13(Gr\,\mathrm{Pr})^{(1/3)}$$

This correlation is used in COBRA-FLX for Reynolds number less than about 10,000. In order to obtain a step-free transition (to avoid numerical instabilities) both values h_{MA} and h_{ST} are calculated and the maximum is used.

Figure Q10-2 shows the Nusselt numbers calculated with the correlations of Sieder-Tate and McAdams using the same boundary conditions used in Figure Q10-1. In Figure Q10-3 the resulting difference between wall temperature and coolant temperature is shown. It should be noted that the wall temperature T_{wall} in the McAdams correlation is based on the heat flux, which is a function of the Reynolds Number. In addition, it should be mentioned that both the Sieder-Tate correlation and the McAdams correlation are members of the BEEST Heat Transfer package described in Reference Q-E, which is incorporated in COBRA-FLX.

Based on this comparison, the use of the McAdams heat transfer correlation in conjunction with Sieder-Tate, as it is implemented in COBRA-FLX, is justified.

Figure Q10-2: COBRA-FLX: Comparison of Nusselt Number based on Sieder-Tate and McAdams

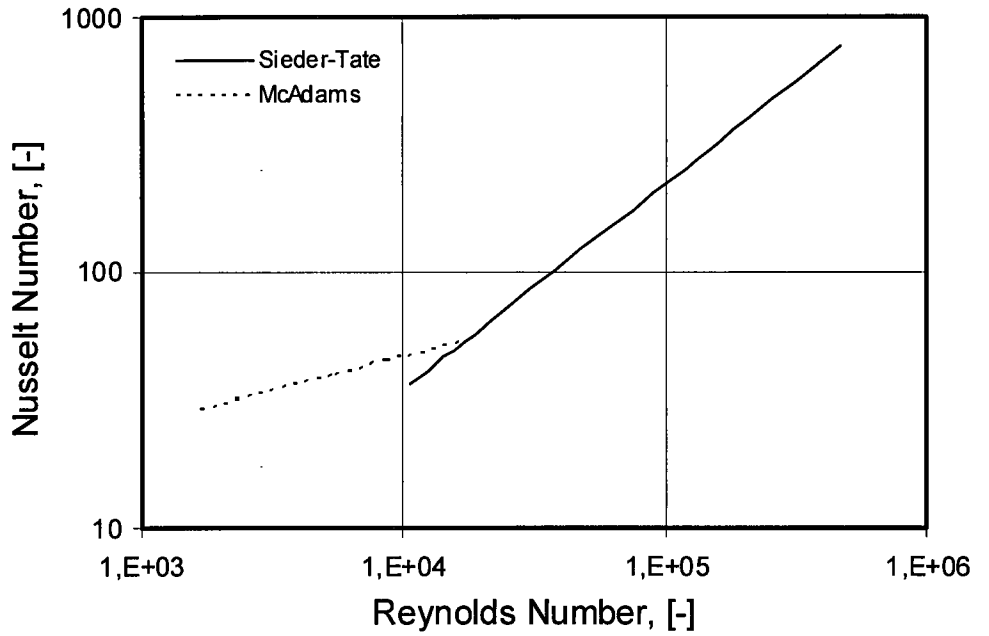

Figure Q10-3: COBRA-FLX: Comparison of Temperature Difference between Wall and Coolant Based on Sieder-Tate and McAdams

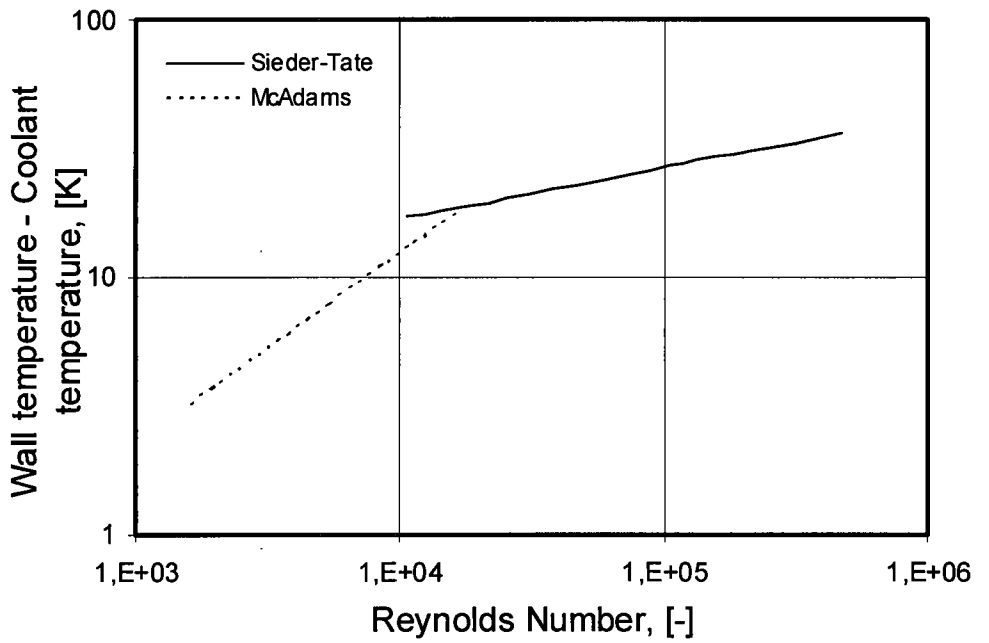

As discussed and agreed upon during the RAI Clarification Conference Call, part (c) of this RAI no longer requires a response.

The Sieder-Tate and Dittus-Boelter single-phase heat transfer correlations agree to within 4 percent over a wide range of Reynolds Numbers typical of reactor operation. The McAdams heat transfer correlation is used to predict a natural convection heat transfer coefficient, which is then compared to the Sieder-Tate heat transfer coefficient and the largest value is used in the COBRA-FLX calculations. The comparisons in this RAI demonstrate that the applications are correct in COBRA-FLX.

The heat transfer correlations and the logic used to select the various heat transfer correlations are defined in Section A.5. The heat transfer logic used is based on the BEEST model defined in Reference Q-E.

References:

Q-A. BAW-10156-A, Rev. 1, LYNXT Core Transient Thermal-Hydraulic Program, B&W Fuel Company, August 1993.

Q-B. BAW-10129-A, LYNX1: Reactor Fuel Assembly Thermal-Hydraulic Analysis Code, Babcock & Wilcox, Lynchburg, Virginia, July 1985.

Q-C. Lahey, R.T. and Moody, F.J. The Thermal-Hydraulics of a Boiling Water Nuclear Reactor American Nuclear Society, La Grange Park, Illinois USA
Second Edition, 1993.

Q-D. Sieder, E.N. and Tate, G.E. Heat Transfer and Pressure Drop of Liquids in Tubes. *Industrial and Engineering Chemistry, Vol. 28 No. 12,* 1936, pp. 1429-1435.

Q-E. Bjornard, T. A.; Griffith, P (1977), *PWR Blowdown Heat Transfer.* Symposium on the Thermal and Hydraulic Aspects of Nuclear Reactor Safety,Volume 1 – Light Water Reactors, American Society of Mechanical Engineers, Atlanta, GA, November 27 - December 2, 1977, pp. 17-39.

Q-F. McAdams, *W.H. Heat Transmission,* Mc Graw-Hill Book Co. Inc,1954.

Q-G. Wehle, F., Velten, R., Kronenberg, J., Beisiegel, A., Pruitt, D., W., Greene, K., R., Farawila, Y., M., 2010. *Stability and Void Fraction Measurements for the ATRIUM™10XM BWR Fuel Bundle.* Proceedings of 2010 LWR Fuel Performance, Top Fuel, Orlando, Florida, USA, September 26-29, 2010.

Q-H. Kolev, N., I., 2006. *Multiphase Flow Dynamics 4 – Nuclear Thermal Hydraulics.* 1st Edition, Springer, ISBN 978-3-540-92917-8.

Q-I. Hori, K., Akiyama, Y., Miyazaki, K., Kurosu, T., Sugiyama, S., 1994. *Transient void fraction measurement in a single channel simulating one channel for a PWR Fuel Assembly.* 10th Proceeding of Nuclear Thermal-Hydraulics, ANS Winter Meeting, pp 56-68.

Q-J. NP-2511-CCMA, Revision 2, VIPRE-01: A Thermal-Hydraulic Code for Reactor Cores, Electric Power Research Institute, July 1985.

Q-K. MIT-EL 81-018, COBRA IIIC/MIT-2: A Digital Computer Program for Steady State and Transient Thermal-Hydraulic Analysis of Rod Bundle Nuclear Fuel Elements, Massachusetts Institute of Technology, June 1981.

Q-L. BNWL-1962, UC-32, COBRA-IV-1: An Interim Version of COBRA for Thermal-Hydraulic Analysis of Rod Bundle Nuclear Fuel Elements and Cores, Battelle Pacific Northwest Laboratories, March 1976.